Structural and Thermal Patterning in 3D Bioprinted Hydrogels for Tissue Engineering

Daniel C Corbett

A dissertation

submitted in partial fulfillment of the

requirements for the degree of

Doctor of Philosophy

University of Washington

2020

Reading Committee:

Kelly R. Stevens, Chair

Ying Zheng

Cole A. DeForest

Program Authorized to Offer Degree:

Bioengineering

University of Washington

Abstract

Structural and Thermal Patterning in 3D Bioprinted Hydrogels for Tissue Engineering

Daniel C. Corbett

Chair of the Supervisory Committee:

Dr. Kelly R. Stevens

Department of Bioengineering

Technologies for orchestrating cell behavior in engineered tissues through environmental or genetic control systems have immense potential to enhance our understanding of multicellular physiology and generate artificial tissues for therapeutic translation. In this work, we present a pair of technological innovations for controlling tissue architecture and cellular gene expression in engineered tissues. First, we describe our stereolithographic approach (SLATE) for bioprinting hydrogel tissues containing multiscale, entangled vascular networks (Chapter 3). Next, we apply perfusive heating of vascular networks to generate thermal profiles within three-dimensional tissues that mediate a spatiotemporal gene expression response through heat shock activation (HEAT, Chapters 4 & 5). Using these technologies, we explore hepatic tissue engineering (Chapter 6), demonstrating both: survival and engraftment of multi-material bioprinted hepatic tissues in a

mouse model of liver injury, and genetic perturbation towards metabolic zonation through exogenous heat regulation.

ACKNOWLEDGEMENTS

First and foremost, I thank my advisor, Prof. Kelly Stevens. Dr. Stevens took me on as her first graduate student. Over the years Dr. Stevens showed a level of commitment to my development, both as a scientist and person, that I doubt I will receive from a mentor again. Thank you, Dr. Stevens, for taking a chance on me.

I thank my committee members who have supported me every step of the way through my research and the graduate school process. Prof. Ying Zheng Prof. Cole A. DeForest, Prof. Buddy Ratner and Prof. Tracy Popowics, I thank you all.

I thank all the past and present members of the Stevens' lab. I consider myself fortunate to have had the opportunity to interact with each of them. Collectively they have fostered an environment that truly makes it a joy to come into lab every day. Chelsea, Mary, Sarah, Parker, Emily, Colleen, Fredrik, Eileen, Wes, Jon, Jinah, Susy, Tara and Olivia, I thank you all.

I thank the Institute for Regenerative Medicine for their scientific and financial support. In particular, I thank Dr. Lil Pabon and Dr. Hans Reincke of the Murry lab for their guidance and support. I would like to thank several professors and staff who provided support financial or equipment. Dr. Nate Sniadecki, Dr. Marta Scatena, Dr. Mike Regnier, Dr. Neal Paragas, Dale Hailey of the ISCRM imaging core, Samer Halabiya and Cami Cordray of BioFAB

Final thanks goes to my parents and all my friends who hold it down for me.

TABLE OF CONTENTS

LIST OF FIGURES

Chapter 1. VOLUMETRIC BIOPRINTING FOR TISSUE ENGINEERING

Tissue function emerges from the hierarchical layering of organized biological response - from the coordinated gene expression of a single cell, to the collective movements of a whole organ[1,2]. Tissue engineering is discipline that seeks to rebuild elements of this structure in order to produce functional human organs *ex vivo*.

Tissue engineering has achieved success in delivering therapeutics for superficial tissue replacements (i.e. skin grafts, corneal sheets)[3]; however, engineering solid organs has been difficult. Foundational methods of biofabrication such as tissue casting[4] and electrospinning[5] are unable to engineer the structural complexity in artificial systems that matches native physiology. 3D printing, a form of additive manufacturing developed in the 1980s[6] refers to the process of making three-dimensional objects from computer-generated files using automated material deposition. In the past decade, revolutions in additive manufacturing have catalyzed research at the 3D printing of human organs (3D bioprinting)[7–9]. As 3D bioprinting has developed and matured it has faced its own roadblocks[10]. Simplistic, monocellular constructs were considered the standard until recently. However, now several groups have shown that innovations in the hardware and materials used for printing can facilitate transformative gains in both tissue structure and resolution. In particular to 3D bioprinting is the movement towards ‘volumetric’ status[11–13]. In volumetric bioprinting biomaterial deposition, degradation or crosslinking occurs in all three geometric planes. This stems from the realization of the need to integrate macroscale tissue structure, that is inherently 3D, into engineered tissues. Here we review the recent

literature in volumetric bioprinting systems that could have transformative potential in tissue engineering.

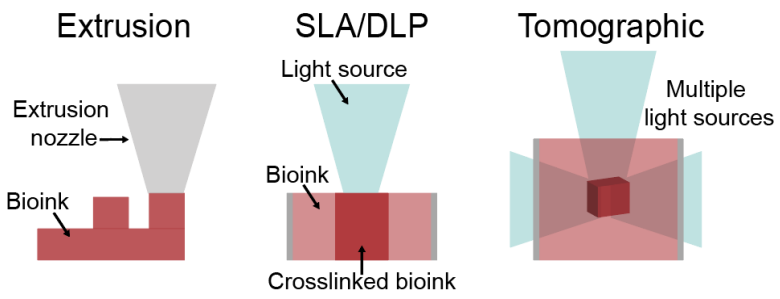

Figure 1.1. Example modalities of 3D bioprinting: 3D bioprinting is advancing from point-by-point fabrication (Extrusion) through layer-by-layer (SLA/DLP) to volumetric (voxel-by-voxel) approaches.

1.1 Support Bath Extrusion Bioprinting

In traditional extrusion bioprinting, an extruder nozzle deposits volume elements ('voxels') while tracing a defined print path on a 2D stage. This presents a constraint on design flexibility because each printed layer needs to be built on top of another layer, The development of the FRESH (freeform reversible embedding of suspended hydrogels) bioprinting method in 2015 by Hinton *et al*[14] demonstrated the first instance of volumetric extrusion bioprinting. By submerging the printer nozzle in a granular gel medium, the authors were able to suspend structures in 3D space long enough for crosslinking to occur. The gel medium could then be dissolved away to release the tissue for handling.

Due to its low technological entry barrier, the FRESH method has been widely adopted by labs and companies[15]. FRESH also has the advantage of being amenable to a wide range of biomaterials. Incorporating crosslinking agents such as HEPES and thrombin in printing support

baths further enables generation of multimaterial prints via orthogonal gelation mechanisms, without additional wash steps. Growth factors can also be incorporated into support baths to promote cellular infiltration and vascularization in bioprinted tissues upon implantation.. A similar technology developed by Skylar-Scott *et al*[16] termed SWIFT 'sacrificial writing into functional tissue' is essentially FRESH with reversed sacrificial and functional components. In SWIFT, the support bath is the tissue component, consisting of a dense solution of cell aggregate spheroids. An extrusion nozzle prints a sacrificial ink into the spheroid solution to create perfusable channels on the order of ~0.5 – 1.0 mm in diameter. In contrast, updated versions of FRESH have demonstrate lower spatial resolution limits of 20 μm when printing acellular collagen[12]. A consensus need for resolution has not been reached. While the collagen strands printed by Lee et al measured 20 μm in diameter it is not known whether these collagen strands exhibit typical nanoscale fibrillar organization, whether this level of organization is achievable, or desirable. Future technologies will likely adapt FRESH and SWIFT as complementary fabrication methods based on optimizing trade-offs between materials and structure.

1.2 PHOTO BIOPRINTING

The first 3D commercial printing systems were based on 'stereolithography' (*stereo*- "solid", *lithography*- *"*stone writing"). These systems in the 1980's combined automatic stage movement with programmable lasers to convert a liquid photoresin into a solid bit-by-bit (voxel-by-voxel)[6]. Today's light-based bioprinting technologies are rooted in the same concept. However, innovations in materials and optical patterning mode have opened a host of tissue engineering applications for *photobioprinting*.

1.2.1 *Laser scanning systems*

The original concept of laser point-rastering remains in use today because the method offers a supreme advantage in spatial resolution (solidification of picoliter (10^{-9} L) volumes). In one demonstration of this, Arakawa *et al*[17] used multiphoton laser excitation to induced localized photopolymer degradation, generating 3D microchannel networks encased within hydrogels at resolutions down to 10 µm. After fabrication, the microchannels were perfused and endothelialized, offering the first demonstration of an engineered blood vessel at capillary level resolution[17]. However, high resolution comes with a tradeoff in lengthy fabrication time. Secondly, for photo chemistries to penetrate deeply in tissue they require optical transparence.

Until these challenges are met, it may be that near-term applications for laser scanning bioprinting lie in printing acellular biomaterials for subsequent cell seedings. This approach was recently demonstrated by Kinstlinger *et al*[18] using selective laser sintering (SLS) of carbohydrate powders for sacrificial channel templating in cell-laden hydrogels. The technology here employs point-source illumination to locally heat and fuse sugar particles into 3D structures. The sintered sugar structure is cast into a hydrogel precursor and dissolved after crosslinking, leaving a relief of the structure in the bulk hydrogel. Using this strategy to fabricate perfusable channel networks in densely cellularized engineered hepatic tissues, the authors were able to preserve hepatic viability and function. Compared to multiphoton excitation, SLS systems have poorer spatial resolution (lower limit ~400 µm) but offer faster print speeds and larger print volumes. Moreover, the sintered objects are compatible with a host of biomaterials and cellularization techniques making sacrificial templating, in general, a more scalable method for tissue engineering.

1.2.2 *Photomask projection systems*

The development of parallelized light projection systems such as digital light processing (DLP)[19] and continuous liquid interface production (CLIP)[20] have dramatically improved the tradeoff between design complexity and fabrication time. DLP and CLIP systems project two-dimensional (*xy*) photomask patterns onto the surface of photocurable liquid resins to simultaneously crosslink entire layers of a printed object. Despite the design flexibility afforded by digital mask projection, many demonstrations of projection-stereolithography for tissue engineering are still limited to simple designs of uniform cross section due to limitations in the photobiopolymer[21–23]. For example, Ma *et al*[22] used a DLP bioprinting system to generate a hexagonal liver tissue models containing two different cell solutions but the total tissue was only two layers thick. Multilayer tissue fabrication in photoprojection bioprinting has hindred by the lack of biocompatible photoabsorbers. In photobased additive manufacturing, spatial resolution is dependent on the optical resolution of the photomask and the physicochemical characteristics of the photoresin[24]. While the digital micro-mirror devices employed in projection light sources enable optical patterning at micron level resolution[24], unintended light propagation in the z-direction can reduce print fidelity. For these liquid bath systems, the light absorption at any point along the light path is dictated by the Beer-Lambert law[24]:

$$E(z) = E_0 \exp\left(-\frac{z}{D_p}\right) \quad (1.1)$$

where E is the light energy, z is the distance along the light path and D_p is the light penetration depth of the photoresin, calculated accordingly[24,25].

$$D_p = \frac{1}{2.3(\varepsilon_I[I] + \varepsilon_A[A])} \quad (1.2)$$

where ε_I and $[I]$ are the extinction coefficient and concentration of the photoinitiator; respectively, and ε_A and $[A]$ are the extinction coefficient and concentration of any photo absorbing agents. Thus, penetration depth is dependent on the concentration and extinction coefficients of photoinitiators and photoabsorbers in the resin. A major push in projection-based methods for bioprinting is to lower the penetration depth to allow for thinner layers in multilayered structures. Chapter 3, as part of this thesis, towards this goal by developing biocompatible, photoabsorbing additives to photobiopolymer solutions.

1.2.3 *Tomographic 3D printing*

Tomographic bioprinting is the computer-aided illumination of a photoresin volume from multiple complementary angles to generate 3D volumes simultaneously[26]. It expands on projection stereolithography by adding more light sources from separate angles to reduce print times while also more accurately targeting print regions. Kelly *et al*[13] demonstrated a version of this called CAL (computer aided lithography) in 2009. Using their method, the authors fabricated features in a host of materials including soft biomaterials (GelMa) at ~1 mm resolution. Since then, other groups are beginning to adopt this approach for tissue engineering[27,28].

There are several benefits to tomographic systems for bioprinting. One being the reduction in print times (down to the order of seconds), that would minimize time spent outside of optimal tissue culture settings. Second, near-simultaneous fabrication across all three-dimensions may enhance crosstalk and connection in engineered tissues. Finally, tomographic printing enables an expanded design space. The technique is capable of printing free-hanging structures allows for the generation of movable actuators such as fluidic valves. In addition, tomographic printing can fabricate objects around pre-existing 3D structures which could be an asset in combinatorial bioprinting.

Resolution still needs to be optimized for this printing modality. As with SLA/DLP systems resolution is dependent on both optical and chemical properties, with the latter imposing stricter limitations. Polymer crosslinking occurs when the cumulative light dose within a voxel exceeds the gelation threshold. Optical resolution using tomographic projection systems can produce cubic voxel elements with edge lengths on the order of 50 μm[27]. On the chemical side, the minimum light exposure time and light penetration depth are vital parameters to optimize for any photoresin. Current state-of-the-art tomographic bioprinting systems can resolve features as small as ~150 μm[27], which matches the resolution of early extrusion bioprinting systems. While cellularized constructs have been printed under tomographic systems, biological functions from encapsulated cells beyond survival and matrix secretion have yet to be demonstrated[27,28]. Further developments will be needed to refine the spatial resolution and biocompatibility of print materials in this promising technology.

1.3 SUMMARY

In summary, tissue engineering is beginning to realize that 2D monolayers are insufficient to drive complex tissue function. New developments in biofabrication, particularly in bioprinting are part of an important class of technologies enabling 3D tissue fabrication.

Chapter 2. REMOTE STIMULI FOR SPATIOTEMPORAL CONTROL OF GENE EXPRESSION

The structural, biochemical and biophysical signals that cells and tissue experience are ultimately transduced in multi-step pathways to coordinate a downstream genetic response[2]. Methods that rely solely on external signal modulation may yield misleading results because many, often unknown, intermediary steps modify intracellular signal transduction prior to gene activation. As a result, technologies for guiding cell behavior through genetic control in engineered tissues have immense potential in fabricating complex organs for therapeutic replacement or regeneration[29].

In recent years, genetic control has advanced beyond the original chemical inducible systems[30] (i.e. Tet on-off) to tether gene regulatory elements to physically targetable exogenous stimuli. This new host of 'remote-control' technologies for gene expression are offering tunable and targeted control far exceeding the capabilities of previous systems. In this chapter we review developments, in pairings of exogenous remote fields to genetic transducers for control of gene expression in engineered cells and tissues.

2.1 OPTOGENETICS

Optogenetics, invented in 2005, is based on the light driven activation of ion channels to control ion flux[31–33]. The method has become an instrumental tool for probing neuron activity and mapping neuronal connections. Subsequent adaptations of this technology are using its cellular scale resolution to target transcriptional control in general cell populations. For example, Ye *et al*[34] developed a system that uses blue-light to trigger melanopsin, a light-sensitive protein, to undergo a conformation change that introduces an intracellular influx of Ca^{2+} ions. The Ca^{2+}

ions form a complex with calmodulin and calcineurin which dephosphorylates the transcription factor nuclear factor of activated T cells (NFAT) and allow it to translocate to the nucleus and begin transcription upon binding to cognate promoters. The authors engineered HEK cells with a genetic cassette in which glucagon-like peptide was downstream of NFAT promoters. Mice that received injections showed reductions in blood glucose levels when the system was activated under light illumination but not under dark.

However, optical patterning faces difficult roadblocks to achieving widespread use in 3D tissue engineering. In human skin and muscle blue light is extinguished at ~1 mm beneath the surface of illuminated tissues[35]. To get past the penetration limits, researchers are develop biocompatible optical implants[36–38], and red-shifted light sensitive proteins[39]. Nonetheless the advantages and availability of optical targeting systems will result in the continued development of more sophisticated optogenetic approaches.

2.2 MECHANOGENETICS

Mechanogenetics[40,41] is a relatively new approach in which mechanical perturbation through magnetic or acoustic fields directly elicits a genetic response. We differentiate here from applications in which a magnetic or acoustic field is used to generate local heating for transcription control.

Magnetic actuation has been implemented widely in tissue engineering for scaffold alignment[42], cell handling[43], or mechanical conditioning of engineered tissues[44]. In these studies, magnetic nanoparticles are targeted to integrin receptors on the cell surface to ‘bulk’ magnetize the cell[45]. Recently, magnetic nanoparticles have also been tagged to intracellular proteins and organelles via protein-nanobody interactions[46,47]. Stanley *et al*[48] demonstrated transcription control by modifying the calcium-NFAT transduction pathway that was employed by Ye *et al*[34].

Here, the molecular transducer for magnetic energy was a magenetosensitive nanoparticle-ion channel complex. HEK293 cells incubated under a standing magnetic field showed significant up to 3-fold upregulation in reporter gene activity and significant declines in blood glucose levels when primed to overexpress insulin in diabetic mice.

Ultrasound waves can be used to locally target tissue volumes on the order of a few cubic mm at tissue depths greater than 5 cm[49]. As a result, focused ultrasound waves have also been applied towards mechanogenetic control in cells and tissues. As with magnetogenetics, acoustogenetics also relies on the pressure induced opening of membrane ion channels to convert mechanical energy into biological response. In one application, Pan *et al*[41] used ultrasound waves to stimulate opening of the mechanosensitive ion channel Piezo1 in genetically engineered peripheral blood mononuclear cells (PBMC) for cancer immunotherapy. The authors were able to achieve a 25% cell killing effect in remotely activated PBMCs remotely when mixed with cells expressing the target receptor *in vitro*.

The specificity of acousto- and magnetosensitive systems remains in question, the nanoparticle-channel complex in Stanley *et al* coulee also activate in response to low frequency radio-waves or mild heating. While the foremost goal in defining inducible gene regulatory systems is to ensure it does not respond to endogenous activation, as remote-control technologies become multiplexed they will need to maintain orthogonality[50]. Furthermore, fold level upregulation remains low in these systems, the absolute magnitude or dynamic range of expression responses necessary to drive biological function may require new transducers or genetic amplification tools[51].

2.3 THERMOGENETICS

Thermogenetics defines the use of thermal energy to affect local temperature changes that produce an expression response. The most commonly employed to date genetic transducers of heat leverages an evolutionarily conserved heat-stress response to control transcription[52,53] (**Figure 2.1**). At homeostasis, heat shock transcription factors (HSF) are bound to molecular chaperones known as heat shock proteins (HSP). Under stress (i.e. hyperthermia) HSPs dissociate into the cytosol prevent protein misfolding and disaggregation. In turn, this frees the HSFs to translocate to the nucleus where they trimerize and bind to heat shock protein promoter sequences to begin transcription. Upon removal of the cellular stressor, HSFs rebind to HSPs and transcription is halted.

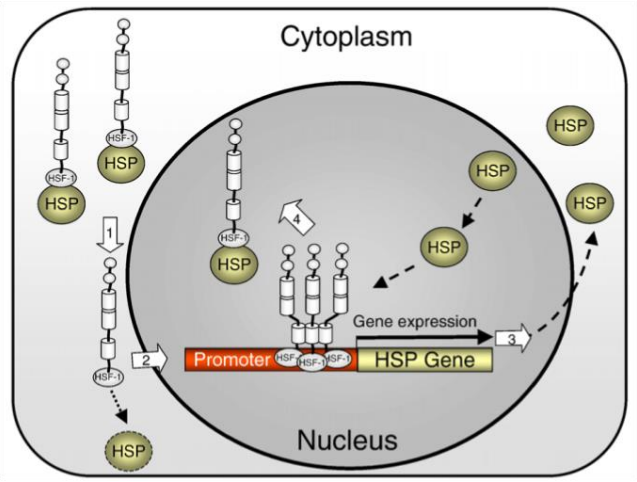

Figure 2.1. Schematic depiction of heat-shock transcription response: Heat shock transcription factors (HSF) and heat shock proteins (HSP) are normally in an inactive state in the cytoplasm. Under stressful conditions, HSFs dissociate, translocate to the nucleus and commence transcription.

The re-engineering of cells with user-defined transgenes downstream of heat shock promoters for conditional gene expression has been in use since the 1980's[52]. In the 21st century,

many research groups are adapting heat-inducible genetic control elements with remote methods of patterning heat energy for biological and tissue engineering applications.

Heat can be applied in various ways, some studies employ simple incubation at hyperthermic temperatures (39 - 45°C) in cell culture incubators or water baths[54,55]. More technologically advanced methods generally rely on one of photothermic stimulation[56–59], high-intensity focused ultrasound (HIFU) [60–62] or magnetic heating[63–65]. In each case, thermal energy is the byproduct of the incident remote field interacting with the local medium within the tissue molecular vibrational motion[66]. The multitude of heat delivery mechanisms opens the door for a variety research groups who have dedicated experience in specific instrumentation to experiment on spatially modulating gene expression. In key work, Deckers *et al*[60] demonstrated the use of MRI-guided HIFU for in vivo spatiotemporal gene activation. Mild heating (43°C) for durations as short as 2 minutes were sufficient to drive localized heat shock induced responses. The ability to pair ultrasound heating with MRI guided temperature tracking to avoid excessive heating is also a key feature of this technology that lends to its clinical application.

As with other remote activation methods, multiplexing gene regulation from a single stimulus can increase the biological efficiency and likelihood to obtain a functional outcome from gene expression. However, coordinated gene responses will require tunable and orthogonal switches. Piraner *et al*[67] demonstrated the use of genetic logic circuits containing heat-responsive elements for multiplexing and bandpass filtering different temperature ranges to evoke different biological responses. More recent work by the same group[68] demonstrated how the core concept of thermal logic circuits and remote activation could be implemented into CAR T cells for cancer immunotherapy. Using heat to drive expression of Cre recombinase, the group was also able to achieve permanent expression from a single heat pulse. As this work demonstrates, the early

work done in elucidating the behavior and kinetics of the heat shock pathway establishes a strong foundation to rationally engineer new heat regulatory gene elements.

Chapter 3. ENTANGLED VASCULAR NETWORKS IN STEREOLITHOGRAPHY PRINTED HYDROGELS

3.1 INTRODUCTION

The morphologies of the circulatory and pulmonary systems are physically and evolutionarily entangled[69]. In air-breathing vertebrates, these bounded and conserved vessel topologies interact to enable the oxygen-dependent respiration of the entire organism[70,71]. To build and interrogate soft hydrogels containing such prescribed biomimetic and multivascular architectures, we sought to use stereolithography, commonly employed to efficiently convert photoactive liquid resins into structured plastic parts through localized photopolymerization[72,73]. Compared with extrusion 3D printing, which deposits voxels in a serial fashion[14,74–77], photocrosslinking can be highly parallelized via image projection to simultaneously and independently address millions of voxels per time step. In stereolithography, xy resolution is determined by the light path, whereas z resolution is dictated by light-attenuating additives that absorb excess light and confine the polymerization to the desired layer thickness, thereby improving pattern fidelity. In the absence of suitable photoabsorber additives, 3D photopatterning of soft hydrogels has been limited in the types of patterns that can be generated[21,22,78,79] or has required complex, expensive, and low-throughput microscopy to enhance z resolution via the multiphoton effect[80–82]. However, common light-blocking chemicals used or photoresist patterning or plastic part fabrication, such as Sudan I, are not suitable for biomanufacturing owing to their known genotoxic and carcinogenic characteristics[83]. Therefore, we hypothesized that the identification of nontoxic light blockers for projection stereolithography could provide a major advance to the architectural richness available for the

design and generation of widely used biocompatible hydrogels Here, we establish that synthetic and natural food dyes, widely used in the food industry, can be applied as potent biocompatible photoabsorbers to enable the stereolithographic production of hydrogels containing intricate and functional vascular architectures. Data presented in the this chapter pertaining to the development of the stereolithographic printing system, characterization of the impact of photoabsorber addition on hydrogel rheology and printing of entangled vascular networks was collected by our collaborators from Rice University: Dr. Jordan S. Miller, Dr. Bagrat Grigoryan and Dr. Samantha Paulsen.

3.2 Materials and Methods

3.2.1 *Development of open-source stereolithography apparatus for tissue engineering (SLATE)*

Our custom-designed stereolithography apparatus for tissue engineering (SLATE) is open-source and contains 3 major components that are attached to an aluminum frame: 1) electronics motherboard (RAMBO; UltiMachine, South Pittsburg, TN) for system control running Marlin firmware; 2) a z-axis with stepper motor linear drive (1 mm/revolution); 3) a 3D printed plastic base with a 45º mirror to reflect the projected images onto the build platform. A build platform containing a glass slide onto which the hydrogels are fabricated is attached onto the Z-stage. The vat consists of a poly(dimethylsiloxane) (PDMS; Sylgard 184, Dow Corning, Midland, MI) coated P100 Petri dish secured by clamps. The PDMS coating prevents sticking of the printed object onto the Petri dish. The base, mirror mount, microcontroller housing, build platform, and Z-platform were 3D printed with an Ultimaker 2 (Ultimaker, Netherlands) in consumer-grade poly(lactic acid) (PLA) plastic filament. The projection device consists of a

PRO4500 Optical Engine (with a display resolution of 1280⇥800 pixels containing a 405 nm LED (Wintech, Carlsbad, CA), attached to a computer for projection of photomasks and motor control. The projector is placed in front of the developed SLATE apparatus and focused to obtain an xy voxel resolution of 50 μm.

3.2.2 *Photosensitive material synthesis, photorheology, and hydrogel fabrication*

Poly(ethylene glycol) diacrylate (PEGDA; 3.4 kDa, 6 kDa) was prepared by reaction with triethylamine and acryloyl chloride in anhydrous dichloromethane under argon overnight[84]. Yields were typically in the range of 80-90% and percent acrylation was >90%, as verified by ^{1}H NMR for the characteristic peak of the PEG methylene protons adjacent to the acrylate, for batch sizes up to 350 g. Lithium phenyl-2,4,6-trimethylbenzoylphosphinate (LAP) was prepared as previously described[85]. Briefly, dimethyl phenylphosphinite and 2,3,6-trimethylbenzoyl chloride were reacted under argon overnight at room temperature followed by addition of 4 molar excess lithium bromide in 2-butanone. The reaction mixture was then heated to 50°C to allow formation of a solid precipitate, cooled to room temperature for 4 hrs, followed by filtration with excess amount of 2-butanone and diethyl ether. Yields up to 90% were achieved for batch sizes up to 30 g. Gelatin methacrylate (GelMA) was synthesized as previously described with slight modifications[86]. Methacrylic anhydride was added dropwise to gelatin dissolved in carbonate-bicarbonate buffer at 50°C for 3 hrs, followed by precipitation in ethanol. The precipitate was allowed to dry, dissolved in phosphate buffered saline (PBS), frozen at -80ºC, then lyophilized for up to 1 week. GelMA was stored at -20ºC until use.

3.2.3 *Hydrogel fabrication by projection stereolithography*

For fabrication of acellular monolithic gels, pre-hydrogel mixtures were prepared containing 20 wt% 6 kDa PEGDA (unless otherwise stated), 34 mM LAP, and photoabsorber

concentration based on desired layer thickness. The pre-hydrogel mixture was transferred onto the PDMS coated Petri dish placed below the build platform, which contains a bonded glass slide onto which the cured gel would attach, was lowered to the first fabrication layer position, and fabrication was managed with Creation Workshop software (http://www.envisionlabs.net/), which controls the apparatus by sending GCode commands for vertical movement of the build platform, and images to the projector, which projects a sequence of photomasks based on the imported 3D model. After printing is completed, the 3D fabricated hydrogel is removed from the glass slide of the build platform with a razor and equilibrated in deionized (DI) water or PBS with multiple washes.

For visualization of topologies, we perfused microfil (Flow Tech Inc, Carver, MA) containing different color dyes into the open channels of fabricated topologies and allowed the microfil to set before taking photographs. Macro photographs were captured with a Canon 5DSR camera (Canon, Tokyo, Japan) and MP-E 65 mm macro lens or EF 100 mm macro lens in RAW mode (50 megapixel) under room lighting or with an Ikan LYRA LED array (Ikan, Houston, TX) or with an Einstein flash (Paul C. Buch, Nashville, TN). Video was captured with the same equipment or with a Sony mirrorless A7SII camera (Sony, Tokyo, Japan) with a Sigma adapter (Sigma, St. Louis, MO) for the MP-E 65 mm lens. Since microfilm contains radiopaque agents, we used microcomputed tomography (μCT) to investigate pattern fidelity. Swollen hydrogels with microfil perfused into the channels were scanned at 0.6 degree steps at 9 μm voxel resolution on a SkyScan 1272 μCT scanner (Bruker, Billerica, MA) equipped with a 11 megapixel camera (XIMEA, Lakewood, CO). Volumetric visualization of scanned hydrogels was achieved by importing reconstructed images (obtained by nRecon Reconstruction software, Bruker, Billerica, MA) into Imaris Image Analysis Software (Bitplane, Zurich, Switzerland).

3.2.4 *Photorheology characterization of hydrogels printed with different photoabsorbers*

Photorheological characterization of hydrogels was performed using an AR-G2 parallel plate rheometer (TA Instruments, New Castle, DE) equipped with a 20 mm diameter parallel plate geometry and an optics attachment in which a PRO4500 projector was used as the light source. For each sample pre-hydrogel mixture (20 wt% 6 kDa PEGDA with 34 mM LAP and various concentration of dye) was loaded onto the bottom plate and the top geometry was lowered to obtain a gap size of 50 or 100 μm. Four-minute time sweep tests were performed, with an angular frequency of 5 rad/s and 0.1% strain, in which the sample was preconditioned for 30 s and then light was initiated for either a short duration (6-40 s) or long duration (120 s) via the PRO4500 (21.5 ± 1.5 mW/cm2). We measured the evolution of the storage modulus of pre-hydrogel mixture containing various concentrations of light absorbers: tartrazine (Sigma, St. Louis, Missouri), curcumin (Sigma), anthocyanin (Badmonkey Botanicals, Tacoma, WA), gold nanoparticles (50 nm, nanoComposix, San Diego, CA).

3.2.5 *Quantifying Tartrazine release*

To measure the release rate of tartrazine from printed hydrogels, three groups of two gels were fabricated (20 wt% 6 kDa PEGDA, 50 μm layer height). One gel from each group was then added to 500 μL of DI water. At 0.5, 1, 2, 4, 8 and 24 hours the water was collected, the volume was measured (since the gels swell and absorb water over time), and the water was replaced with 500 μL of fresh DI water. To calculate the amount of tartrazine released at each time point, the absorbance of each sample at 430 nm was compared to that of a standard curve. Next, to determine the amount of tartrazine remaining in each gel after the fabrication process, the second gel from each group was added to 1 mL of 1 M sodium hydroxide and degraded over 48 hours. The absorbance of the degraded gels was then compared with a standard curve of tartrazine that

had been exposed to the same pH conditions. The amount of tartrazine remaining in printed gels was then used to calculate the total percentage of tartrazine released from the gels over time.

3.2.6 *hMSC and HEK293 3D Viability*

For 3D hMSC encapsulation studies, we fabricated cylindrical hydrogels (diameter = 6 mm; height = 1 mm) of different material compositions to assess viability and differentiation (with xanthan gum in the pre-hydrogel solution to prevent cell settling) (fig. S13). For short-term cell viability determination, we fabricated gels out of 15 wt% GelMA along with a mixture of 12 wt% 6 kDa PEGDA + 8 wt% GelMA (with or without tartrazine) with hMSCs (p3-4) at $1x10^6$ cells/mL or HEK293s (p6-10) at $6x10^6$ cells/mL. To aid in homogeneous distribution of cells throughout the height of the gel, xanthan gum (Sigma), a natural thickening agent, was added into the pre-hydrogel solution to obtain a neutrally buoyant suspension. The gels were rinsed with media, removed from the build platform, and transferred into a well plate. For hydrogels fabricated with tartrazine, media was replaced 3 times within the first 2 hours of incubation. After either 2 or 24 hr incubation gels were rinsed with PBS and viability of encapsulated cells was determined using Live/Dead assay (Life Technologies, Carlsbad, CA) according to the manufacturer's instructions. Gels treated with 70% ethanol prior to staining served as negative controls. Fluorescent imaging was performed on a Nikon Eclipse Ti inverted epifluorescent microscope (Nikon Instruments Inc., Melville, NY) equipped with a Zyla 4.2 sCMOS camera (Andor, South Windsor, CT). Live and dead cells were quantified using Nikon NIS Elements software.

3.2.7 *Statistics*

Data in graphs are expressed as the SE or SEM ± SD, as denoted in figure legends. Statistical significance was determined using two-tailed Student's t test for two-way comparisons

or one-way ANOVA or two-way ANOVA followed by Dunnett's, Sidak's, or Tukey's multiple comparison test.

3.3 RESULTS

3.3.1 *Development of SLATE bioprinting apparatus*

To 3D print hydrogels we developed the Stereolithographic Apparatus for Tissue Engineering (SLATE) bioprinting method (**Figure 3.1 A-C**). In SLATE, a digital micromirror device (DMD) in the printer's light source patterns each photomask onto the build platform. The DMD is a rectangular array (1280x800) of square (8 µm x 8 µm) micromirrors that can be individually rotated thereby controlling the "on-off" state of individual pixel (**Figure 3.1 B**). Slicing software converts the 3D model file into a series of sequential photomasks and the model is constructed using layer-by-layer light polymerization (**Figure 3.1 C)**.

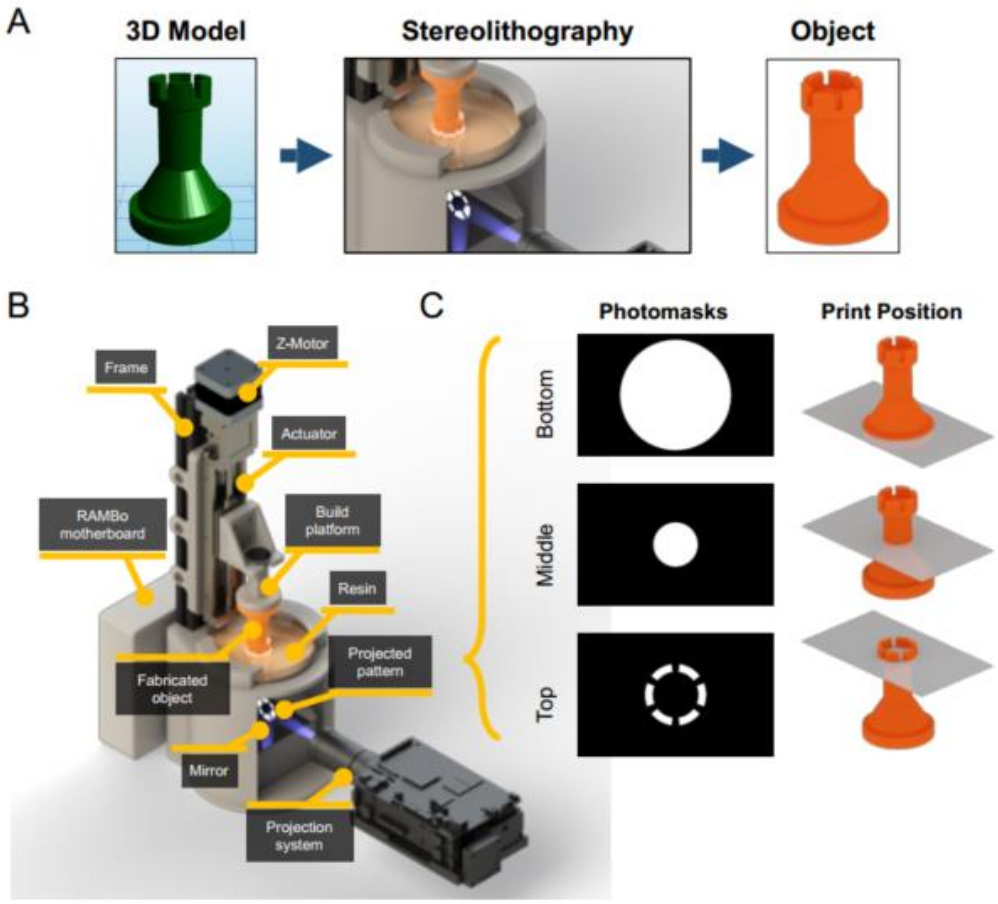

Figure 3.1. Stereolithography Apparatus for Tissue Engineering (SLATE). **(A)** A schematized workflow for fabrication of 3D objects by projection stereolithography. Photomasks corresponding to a 3D model are projected into a vat containing a photosensitive liquid solution. Upon completion of sequential layer-by-layer photopatterning, a 3D object is obtained. **(B)** 3D rendering of the designed projection stereolithography apparatus. The system consists of a motor, controlled by an actuator, onto which the build platform is attached. The back of the printer houses the RAMBO motherboard which controls the motor and performs input–output with any additional sensors or switches. The front of the printer contains a mirror placed 45º to reflect incident patterns from a projector onto a dish containing the photosensitive materials. All o↵-white colored parts correspond to parts that were 3D printed out of consumer-grade poly(lactic

acid) (PLA) plastic filament. **(C)** Schematic demonstrating photomasks (left) that are generated at different locations along the height of the 3D rook model

3.3.2 *Food dye photoabsorbers permit stereolithographic fabrication of 3D hydrogels with open channels*

We set out to identify biocompatible photoabsorbers that enable the stereolithographic production of hydrogels containing perfusable vascular elements. We initially sought to generate monolithic hydrogels, composed primarily of water and poly(ethylene glycol) diacrylate (PEGDA, 6 kDa, 20 wt%), with a 1 mm cylindrical channel oriented perpendicular to the light projection axis (**Figure 3.2 A**). Importantly, the absence of photoabsorbers even in this trivial design prohibits the formation of a patent vessel (**Figure 3.2 B**). This is because the dilute nature of aqueous hydrogel solutions necessitates increased time to reach gel point, enhances light scattering and increases the diffusion of free radicals. We determined that aqueous pre-hydrogel solutions containing tartrazine (yellow foodcoloring FD&C Yellow 5, E102), curcumin (from turmeric), or gold nanoparticles can each yield hydrogels with a patent vessel (**Figure 3.2 B**). From these, we selected tartrazine as a photoabsorber for further studies due to three provided advantages over its competition (1) its proven low toxicity in humans as evidenced by its broad utility in the food industy[87], (2) a match between tartrazine's absorbance peak with the wavelength emitted by our light source (**Figure 3.2 C**), and (3) the optical transparency of hydrogel's prepared using tartrazine. Tartrazine, being a hydrophilic dye, elutes readily (up to 70% within 3 hours for small gels) in water or physiologically relevant saline solutions rendering hydrogels near optically transparent (**Figure 3.2 D**). To understand how this photoabsorber affects the gelation kinetics of photopolymerizable hydrogels, we performed photorheological characterization with short-duration light exposures which indicate that tartrazine causes a dose-

dependent delay in the induction of photocrosslinking (**Figure 3.2 E**). Saturating light exposures that extend beyond the reaction termination point demonstrate that tartrazine addition did not ultimately interfere with the reaction because hydrogels eventually reached an equivalent storage modulus independent of the additive concentration.

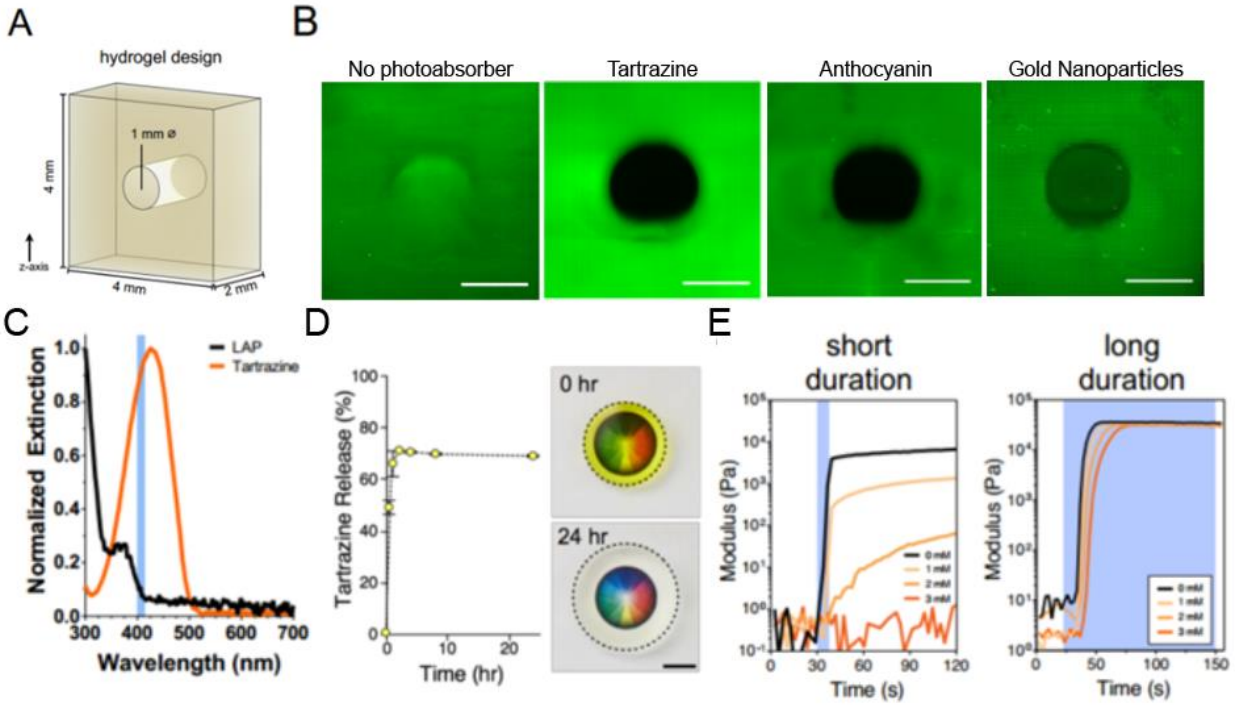

Figure 3.2. Selection of tartrazine for fabrication of monolithic hydrogels with patent vessels: (A) A monolithic hydrogel with a horizontal vessel can be fabricated by projection stereolithography only with suitable photoabsorbers added to the pre-hydrogel solution which can minimize excess light penetration into the nascent vessel (schematized). **(B)** Projection stereolithography with tartrazine yields hydrogels with minimal excess crosslinking in the vessel lumen (asterisk) and shown as line plot inset (bar = 1 mm). **(C)** Absorbance spectra of LAP photoinitiator and photoabsorber tartrazine. The absorbance spectra of tartrazine encompass our

light source (vertical bar at 405 nm) which can be used to initiate photocrosslinking via the LAP photoinitiator. **(D)** Photorheology during short duration (left) and long duration (right) light exposures (blue shaded region) demonstrates that tartrazine addition (0-3 mM) slows the induction of crosslinking but does not ultimately interfere with gelation (lines are averaged plots, N = 3). (**E**) Hydrogels release up to 70% tartrazine within hours (exemplified by photos of gels above a color wheel, inset, bar = 5 mm), making fabricated hydrogels suitable for color and fluorescence imaging.

3.3.3 *Fabrication of entangled and complex vascular networks in 3D hydrogels*

Next, we assessed whether photoabsorber addition could impart new architectural freedoms to the fabrication of vascular networks in photoactive materials. Solid organs contain distinct fluidic networks that are physically and chemically entangled. However, fabrication of multivesicular topologies in soft hydrogels has proved difficult due to the challenge in preventing intersection between vascular architectures. To parametrically scan the design space of complex vascular blueprints we developed a design framework around mathematical space-filling and fractal topology algorithms. We then fabricated a selection of hydrogels (20 wt%, 6 kDa PEGDA) containing entangled vascular networks based on 3D mathematical algorithms: a helix surrounding an axial vessel (**Figure 3.3 A**), 1° and 2° Hilbert curves (**Figure 3.3 B**), a bicontinuous cubic lattice (based on a Schwarz P surface) (**Figure 3.3 C**), and a torus entangled with a torus knot (**Figure 3.3 D**).

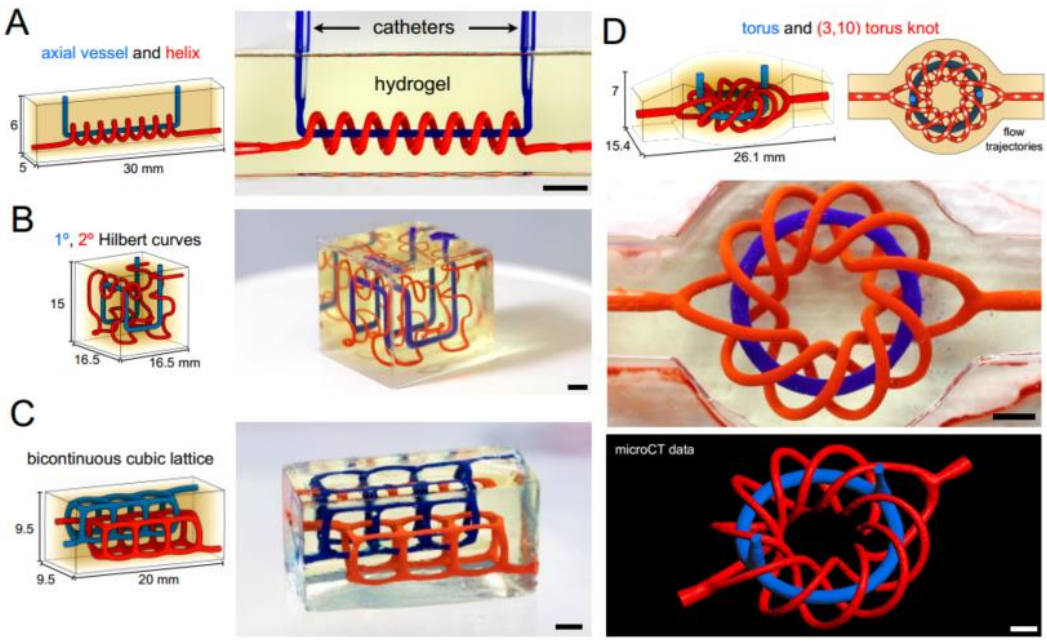

Figure 3.3. SLATE fabrication of entangled vascular networks: (**A-D**) Adaptations of mathematical space-filling curves into entangled vessel topologies within hydrogels (20 wt% PEGDA, 6 kDa): (**A**) axial vessel and helix, (**B**) interpenetrating Hilbert curves, (**C**) bicontinuous cubic lattice, and (**D**) torus and (3,10) torus knot (bars = 3 mm).

3.3.4 *SLATE fabrication impact on cell viability*

Finally, we subjected primary human mesenchymal stem cells (hMSCs) to SLATE fabrication (with mixtures of PEGDA and gelatin methacrylate), and show that cells within cylindrical fabricated hydrogels remain viable (**Figure 3.4**). hMSC viability in SLATE fabricated hydrogels was statistically equivalent between hydrogels with or without tartrazine at up to 10 mM concentration (**Figure 3.4 A**). Cell viability was also unimpacted by LAP concentration up to 50 mM for incubation times of 30 – 60 min (**Figure 3.4 B**). Longer incubation times (2 or 24 hours) for hMSCs in printed hydrogels of methacrylated gelatin

(GelMa), or PEGDA-GelMa mixtures with and without tartrazine showed > 80% viability across all testing groups (**Figure 3.4 C)**. For each hydrogel material, a slight (3 – 5%) drop in viability was observed from 2- to 24- hour incubation times. Finally, Calcein AM/Ethidium homodimer Live/Dead staining of HEK293T cells encapsulated in printed cylinders of PEGDA-GelMa with tartrazine (10.0 mM) qualitatively demonstrated cells remain viable in printed constructs (**Figure 3.4 D**).

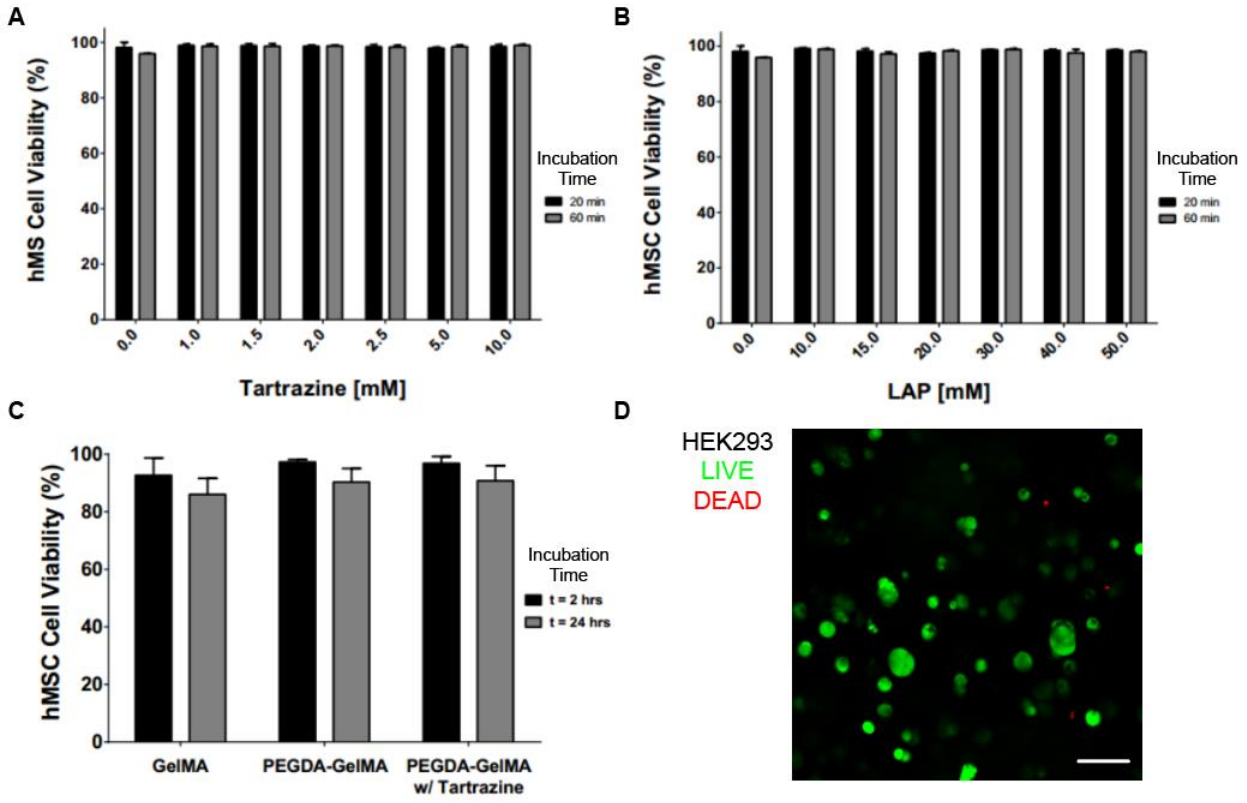

Figure 3.4. Inclusion of tartrazine does not affect viability of human mesenchymal stem cells: (**A,B**) Human mesenchymal stem cells (hMSCs) incubated with 1-10 mM tartrazine (**A**) and 10-50 mM LAP (**B**) for 20 and 60 min resulted in high cell viability. (**C**) hMSCs fabricated in cylindrical hydrogels demonstrated high cell viability in bioactive hydrogels (N = 3, data are shown as mean ± standard deviation). (**D**) Calcein AM/Ethidium homodimer (Live/Dead) staining for HEK293T cells encapsulated in cylindrical hydrogels

3.4 Discussion And Conclusions

We have identified readily available food dyes that can serve as potent photoabsorbers for biocompatible and cytocompatible production of hydrogels containing functional vascular topologies for studies of fluid mixers, valves, intervascular transport, nutrient delivery, and host engraftment. With our stereolithographic process, there is potential for simultaneous and orthogonal control over tissue architecture and biomaterials for the design of regenerative tissues.

Chapter 4. DEVELOPMENT THERMOFLUIDIC HEAT PATTERNING IN HYDROGELS

4.1 INTRODUCTION

Having demonstrated the ability of the SLATE to pattern architecturally complex spatial structures, we next sought to expand on this capability by patterning physical stimuli in solid 3D hydrogels. The ability to pattern physical stimuli (light, heat, magnetic fields) in engineered tissues has numerous applications in tissue engineering directing cell behavior[1]. As opposed to other forms of patternable physical energy, we elected to adapt the SLATE method for heat patterning based on (1) the ability of heat to penetrate deeply (> 5 cm) within tissues, (2) the availability of real-time heat measuring/monitoring devices (thermocouples, infrared thermography) and (3) the availability of heat-inducible genetic expression systems that can activate in biocompatible, mild hyperthermic temperature ranges (40 – 45 ºC).

4.2 MATERIALS AND METHODS

4.2.1 *Development of Thermofluidic heating system in 3D printed hydrogels*

To control temperature distribution in perfused hydrogels, an in-line fluid heater was developed to prewarm perfusate solutions before infusion in hydrogel channel networks. The fluid heater consists of four components: (i) an adjustable dc Power Supply (Yescom USA Inc., City of Industry, CA), (ii) a cylindrical cartridge heater (Uxcell, Hong Kong), (iii) perfusate tubing (peroxide-cured silicone tubing, Cole Parmer, Vernon Hills, IL), and (iv) a syringe pump (Harvard Apparatus, Holliston, MA). To construct the in-line fluid heater, perfusate tubing was connected to the syringe pump for flow rate control, while the cartridge heater was connected to the power supply for heating control. Perfusate tubing was then wounded around the cylindrical

cartridge heater, allowing for heat transfer from the heater into the flowing perfusate. The temperature of the fluid was then controlled by changing the flow rate or heater power. In all studies, we used PBS (Thermo Fisher Scientific, Hampton, NH) for the perfusate solution.

4.2.2 *Hydrogel fluidic connections*

To establish a fluidic connection between the heating system and hydrogel channel networks, we used custom-designed 3D printed perfusion chips printed on a MakerGear M2 3D printer MakerGear, Beachwood, OH) in consumer-grade poly(lactic acid) plastic filament. Perfusion chips were fabricated with (i) an open cavity to insert 3D bioprinted hydrogels and (ii) attachment ports for fluid-dispensing nozzles. The outflow of the fluid heater was fitted with a male luer hose barb (Cole Parmer) connected to a flexible tip, polypropylene nozzle (Nordson EFD, East Providence, RI) and inserted into 3D printed attachment ports. Hydrogels were then inserted to perfusion chips, and proper fluidic connections were ensured before beginning perfusion.

4.2.3 *Infrared thermography*

Fluid temperature and heat distribution were measured in perfused hydrogels by infrared thermography. Images were acquired by an uncooled microbolometer-type infrared camera (FLIR A655sc, Wilsonville, OR) that detects a 7.5- to 14.0 μm spectral response with a thermal sensitivity of <0.05°C and analyzed for temperature values using the FLIR ResearchIR software (Wilsonville, OR).

4.2.4 *Computational models*

We built finite element models of perfused hydrogels in COMSOL 4.4 software (COMSOL AB, Burlington, MA). Simulations were run under transient conditions using the "Conjugate heat transfer" module and 3D printed hydrogel and housing geometries to predict the

temperature distribution. The model was based on (i) forced convective heat transfer from the perfusion channel to the hydrogel volume and (ii) conductive heat transfer within the hydrogel volume. Equation for (i):

$$\rho C_\rho \frac{\partial T}{\partial t} + \rho C_\rho \boldsymbol{u} \cdot \nabla \mathrm{T} = \alpha_p T \left(\frac{\partial p_A}{\partial t} + u \cdot \nabla p_A \right) + \tau : S + \nabla \cdot (k \nabla T) \qquad (4.3)$$

Where ρ is the fluid density, T is the temperature, Cρ is the heat capacity at constant pressure, u is the velocity field, α is the thermal expansion coefficient, pA is the absolute pressure, τ is the viscous stress tensor, S is the strain rate tensor, k is the fluid thermal conductivity and Q is the heat content.

Equation for (ii)

$$\rho C_p \frac{\partial T}{\partial t} = \nabla \cdot (k \nabla T) + Q \qquad (4.4)$$

Where ρ is the hydrogel density, Cρ is the heat capacity at constant pressure, T is the temperature, k is the hydrogel thermal conductivity and Q is the heat content. Material properties of both the hydrogel and perfusate were modeled as water. Heat flux boundary conditions were included to model heat loss to the ambient environment, heat transfer coefficients of 5 and 30 W/(m^2*K) were applied to the sides and upper boundaries of the hydrogel respectively, with an infinite temperature condition of 22.0ºC applied for all boundaries. Boundary temperature and fluid inflow conditions at the channel inlet were used to simulate the effect of changing perfusate temperature and flow rate, respectively. Model geometry was manipulated for studies on channel length and channel branching. Prescribed external temperature was varied for ambient temperature studies.

4.2.5 *Statistics*

Data in graphs are expressed as the SE or SEM ± SD, as denoted in figure legends. Statistical significance was determined using two-tailed Student's t test for two-way comparisons or one-way ANOVA or two-way ANOVA followed by Dunnett's, Sidak's, or Tukey's multiple comparison test.

4.3 RESULTS

4.3.1 *Development of thermofluidic patterning system in 3D printed hydrogels*

To pattern heat in 3D hydrogels created by the SLATE printing method we developed an approach we term Thermofluidics. Thermofluidics is a method for mesoscale spatiotemporal regulation of temperature in 3D hydrogels that is amenable with SLATE. Thermofluidics exploits volumetric fluid-based heat transfer from perfusable, fluidic channel networks encased in 3D printed hydrogels. Channel networks are perfused with precisely heated fluid from a power-supplied heating element (**Figure 4.1**).

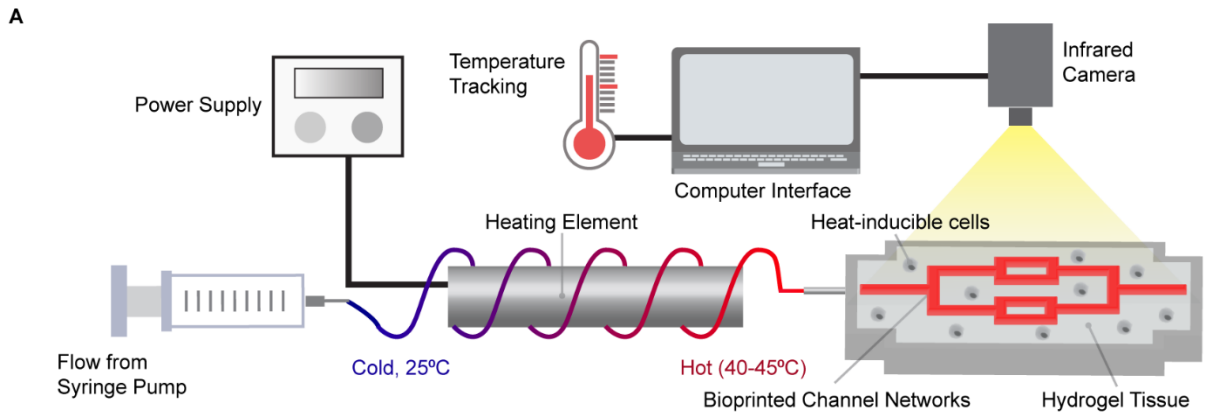

Figure 4.1. Thermofluidic heating in 3D bioprinted hydrogels. (**A**) Schematic of thermofluidic workflow. A biocompatible fluid flows around a power supplied heating

element to preheat the fluid before entry in perfusable channel networks within hydrogel tissue constructs laden with heat-sensitive cells. During perfusive heating, hydrogel temperature is continuously monitored using an infrared camera.

4.3.2 *Thermal characterization in single channel hydrogels*

We sought to match heating in our system to the 'mild hyperthermic' temperature window required to activate most mammalian heat shock promoters. To do this, we first needed to characterize the relation between heating element power and fluid flow rate. We incrementally increased flow rate over a range of heating element powers and measured fluid temperature at the point of heater outflow (**Figure 4.2 A**). Our characterization revealed that higher increasing the heating element power increased fluid outlet temperature at all flow rates. Across all heater powers tested, perfusate temperature increased sharply in the range of 0.2 – 0. 8 mL min^{-1}, peaked, and steadily declined. The drop in fluid temperature across flow rates > 0.8 mL min^{-1} is attributed to the shortened contact time between the perfusate and the heating element resulting in lesser overall heat transfer.

We next implemented the perfusate temperature values observed from each flow rate at 13.5-W heater power into a computational model of single-channel hydrogel heating because this heater power generated hydrogel temperatures that fit in the range of mild hyperthermia (**Figure 4.2 B**). Computational simulations agreed with experimental data showing peak heating occurs in the range of 0.5 – 1.2 mL min^{-1} but not for slower or faster flow rates.

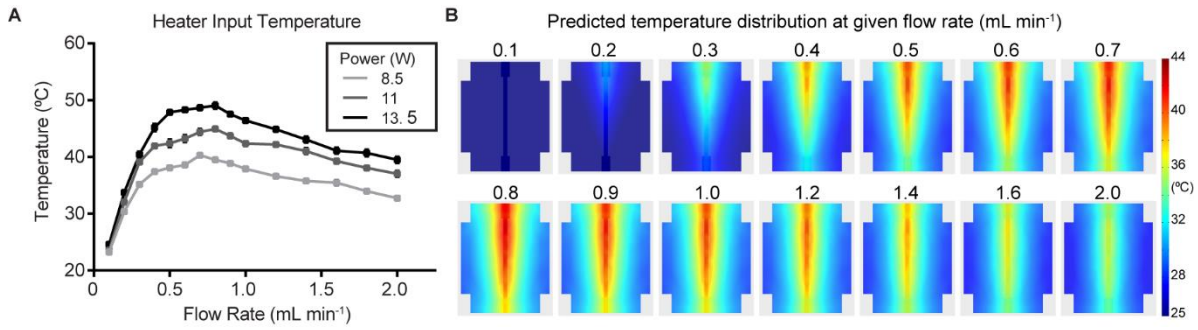

Figure 4.2. Physical and computational characterization flow rate in fluidic hydrogel heating system: (**A)** Measurements of fluid temperature at heater outflow indicate that both fluid flow rate and heating element power affect hydrogel inlet temperature (n = 3, data represent mean temperature ± standard error). (**B**) Full dataset of finite element modeling predictions of temperature distribution in perfused hydrogels at flow rate and temperature combinations from the 13.5 W curve in A. Hyperthermic temperatures are predicted at the hydrogel surface with perfusion flow rates ranging 0.4 – 1.6 mL min^{-1}.

During perfusion, heat is transferred from fluidic channels to the bulk through convection and conduction, resulting in thermal gradients throughout the bulk volume. The perfusate input temperature is known to govern the rate and magnitude of heat transfer, while fluid flow rate influences the thermal profile. Within this window, we observed that flow rates of 0.5 and 1.0 ml min^{-1} produced subtle differences in the shape of thermal profiles, despite roughly equivalent input temperatures. Thus, these flow rates provided a set of conditions to further examine the effects of flow rate on heat transfer.

We therefore performed experimental validation studies of perfused single-channel hydrogels at 0.5 or 1.0 ml min^{-1} and analyzed the steady-state thermal profiles from infrared images (**Figure 4.3 A**). Experimental temperature measurements (solid lines) and computational simulation predictions (dashed lines) showed agreement when measured both orthogonal (**Figure**

4.3 B) and parallel (**Figure 4.3 C**) to channel flow. Both physical measurements and simulations demonstrated thermal gradients in the hydrogel. Temperature along the channel was better maintained under flow at 1.0 ml min^{-1} compared to flow at 0.5 ml min−1 and flow at 0.5 ml min^{-1} promoted more heat transfer at the channel inlet.

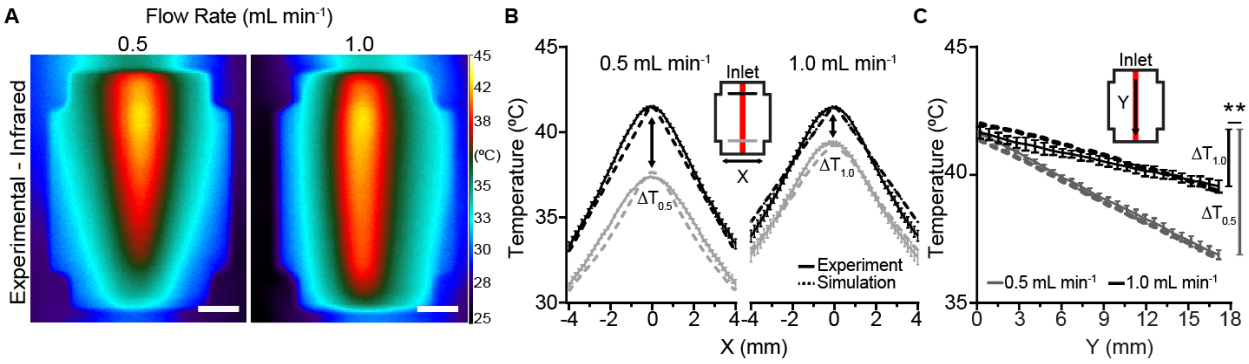

Figure 4.3. Effect of perfusion flow rate on thermal profile: (A) Hydrogels were experimentally perfused at flow rates of 0.5 and 1.0 ml min^{-1} and imaged using infrared thermography. Scale bars, 5 mm. (**B**) Hydrogel temperature plotted orthogonal (x) to the flow direction at inlet and outlet positions show agreement between thermal gradients in computational and experimental measurements (computational, dashed lines; experimental, solid lines). (**C**) Hydrogel temperature plotted parallel (y) to flow direction demonstrates a larger temperature drop from inlet to outlet (y) during flow at 0.5 ml min^{-1} ($\Delta T_{0.5}$) compared to flow at 1.0 ml min^{-1} ($\Delta_{T1.0}$) in computational and experimental models (computational, dashed lines; experimental, solid lines; n = 5, data are mean temperature ± standard error, **P < 0.01 by Student's t test).

To further computationally explore the potential spatial design space for a single-channel system, we assessed how varying channel length, spacing and ambient temperature affect the thermal profile in our model. Predictions showed that single channels up to 30 mm long achieved hyperthermic temperatures (40° to 45°C) along their entire length, with outlet temperatures falling out of the hyperthermic range at greater lengths (**Figure 4.4 A**). Spatial heat distribution was only marginally affected within the ambient temperature range used in our studies here (20° to 22°C; **Figure 4.4 B**), but more substantive increases in ambient temperature (e.g., to 30, 37°C) produced wider spatial gradients in hyperthermic range (**Figure 4.4 B**). Computational models of a similar bifurcating channel geometry further demonstrated how simple changes to parameters such as channel spacing can alter spatial thermal profile, achieving hyperthermic temperature ranges between channel branches at the inlet spaced up to 20 mm from another (**Figure 4.4 C**). Together, these studies showed that the rules of heat transfer could be leveraged to predict thermal spatial profiles in perfused hydrogels and that these profiles could be finely tuned by varying parameters such as flow rate, channel length, and input and ambient temperature.

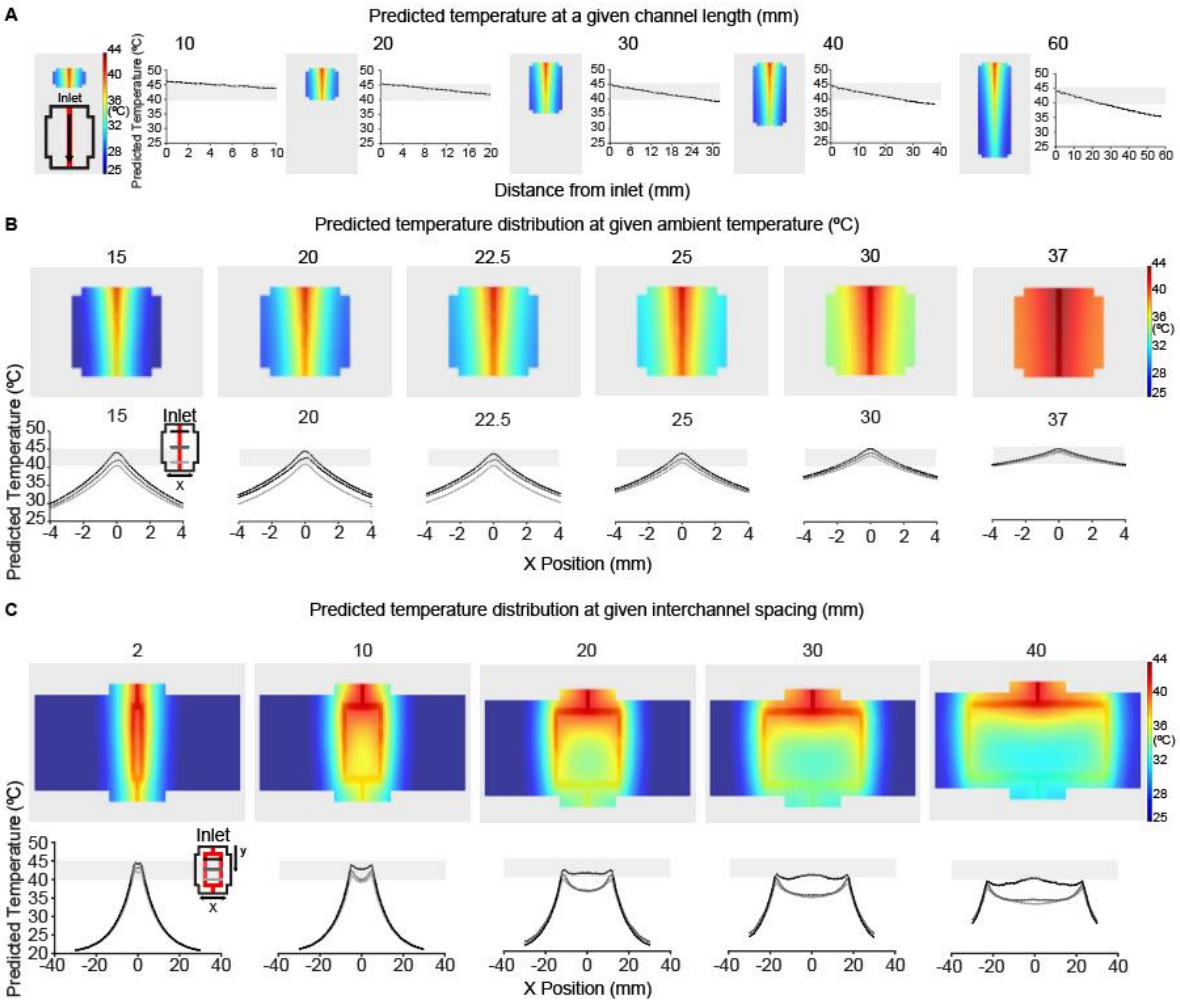

Figure 4.4. Computational characterization of thermofluidic dimensions and ambient conditions: (**A**) Finite element modeling predictions of temperature distribution in perfused gels of varying channel length predict that hydrogels up to 30 mm long achieve hyperthermic temperature ranges along their full length (hyperthermic region (40 – 45 ºC), gray shading). (**B**) Finite element modeling predictions of temperature distribution in perfused gels at varying ambient temperature. (**C**) Finite element modeling predictions of temperature distribution in perfused branched channel gels at varying interchannel spacing. Bifurcating channel geometries with daughter branches spaced at interchannel distances from 2 – 40 mm were computationally modeled (top). Hyperthermic temperature ranges are predicted across hydrogel width (x)

between the channels at inlet (black), middle (dark grey) and outlet (light grey) positions for 2 – 10 mm interchannel spacings (bottom).

4.3.3 *Kinetics of thermofluidic heating*

We next tested whether thermofluidics could precisely regulate tissue temperature over prolonged periods of time by maintaining steady-state thermal profiles in perfused hydrogels. To do this, we first printed hydrogels that contained a single channel (**Figure 4.5 A**). We then perfused precisely heated fluid through this channel while tracking hydrogel temperature in real-time using infrared thermography (**Figure 4.5 B**). Upon initiating perfusion, we observed that hydrogel temperature underwent an initial ramp-up phase (~5 min) followed by a steady-state plateau in which temperature deviated by <±0.4°C/min at three separate regions measured across the hydrogel (**Figure 4.5 B, right**)

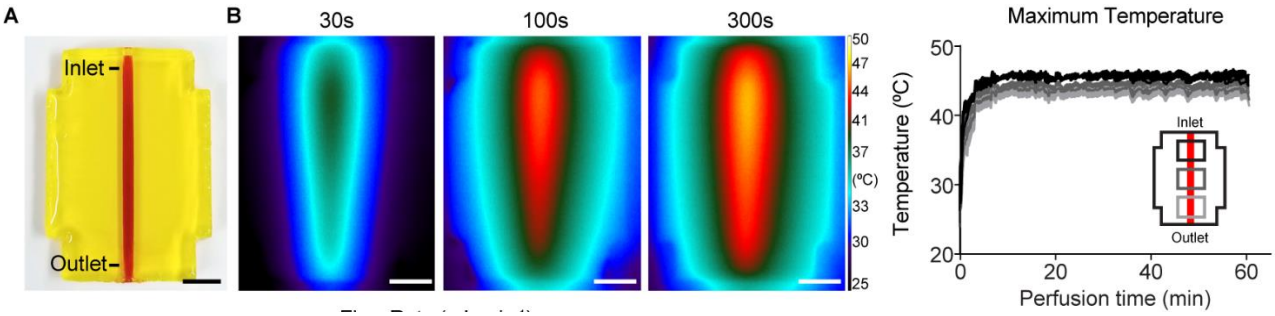

Figure 4.5. Temporal characterization of heating in perfused hydrogels: (**A**) Photograph of a single-channel bioprinted hydrogel used for initial thermal characterization. Scale bar, 5 mm. (**B**) Representative infrared images from controlled perfusion of heated fluid through the channel over time (left). Scale bars, 5 mm.

4.3.4 *Complex thermal architecture patterning*

To illustrate that heat patterning in thermofluidically perfused hydrogels are dictated by the channel network architecture, we fabricated a range of different network geometries: a single straight channel (Axial), branching network geometries (Branched, Grid), multiple inflection points (Serpentine) and 3-dimenstional flow path (Cube) (**Figure 4.6**). During heated perfusion, hydrogel temperature is monitored in real-time using an infrared camera. In each example we observed that heat transfer followed the fluid path with highest temperature occurring near the flow inlet. Thus, thermofluidics facilities heat transfer from the channels into the bulk hydrogel and enables architectural heat patterning in hydrogels.

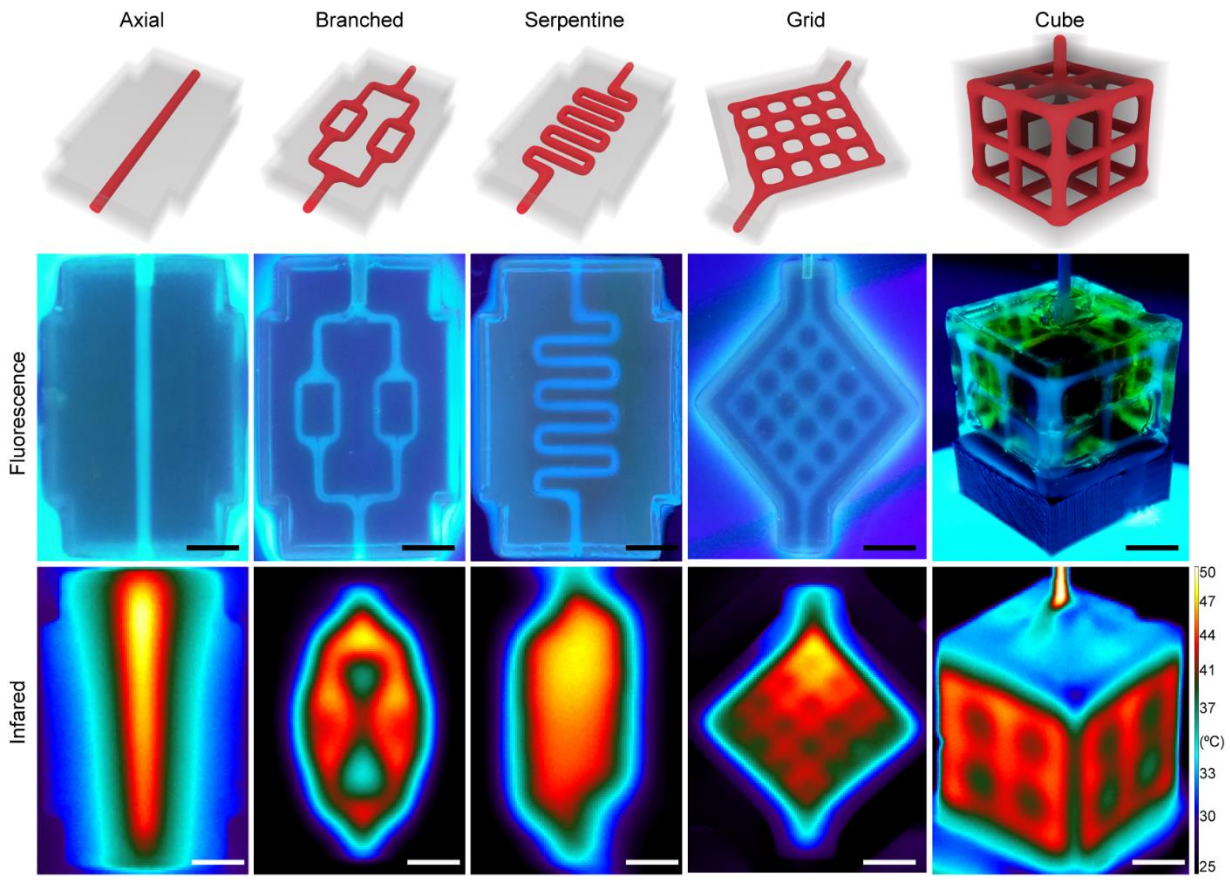

Figure 4.6. Thermofluidic heating in 3D bioprinted hydrogels: Perfusable channel networks of varying spatial geometries can be bioprinted within biocompatible 3D hydrogels. Top: 3D rendering of network architectures. Middle: Hydrogel channels infused with tonic water fluoresce when imaged under ultraviolet backlight. Bottom: Infrared thermography of heat-perfused hydrogels demonstrates that during perfusion, heat traces the path of fluid flow and dissipates into the bulk hydrogel. Scale bars, 5 mm.

4.4 Discussion And Conclusions

While our studies here reveal the potential power of HEAT for gene patterning, the first-generation system presented here does have limitations in its ability to fully control heat transfer both spatially and temporally. In our studies here, we found that channels up to 30 mm long (but

no longer) could achieve hyperthermic temperature ranges along the entire channel length. Furthermore, the effect of heat-mediated stimulation on gene expression was transient. These limits could be overcome through a variety of design modifications. For example, the hydrogel or perfusate's thermal conductivity could be increased by materials engineering to extend patterning area or length, such as by cross-linking metal nanoparticles into the polymer backbone as has been done before for other applications[88]. To achieve different activation temperatures or dynamics, further genetic engineering of the heat shock promoter or other heat-activatable gene switches could be used[65]. Thus, we envision that our initial system here will establish an important foundation that leads to a new family of studies that will ultimately describe a far greater "design space" for thermofluidic patterning

Chapter 5. HEAT (HEAT ENGINEERED ACTUATION OF TRANSCRIPTION) SYSTEM FOR SPATIOTEMPORAL CONTROL OF GENE EXPRESSION IN ARTIFICIAL TISSUES

5.1 INTRODUCTION

Cells transform noisy environmental signals into spatial and dynamic gene expression patterns that guide biological form and function. Information describing how these transcriptional networks are patterned is exploding because of revolutions in single-cell RNA sequencing and spatial transcriptomics. Recapitulating this spatiotemporal information transfer in three-dimensional (3D) tissue settings remains a pivotal yet elusive goal of diverse fields, such as tissue engineering[89], synthetic biology[90,91], and developmental biology[92]. To control gene expression, biologists have developed diverse technologies to rewire cells at the genetic level, such as gene knockout, inhibition, overexpression, and editing[93–95]. To further enable spatial and dynamic control of gene expression, several of these tools have been adapted to be triggered by exogenous stimuli such as light (e.g., optogenetic transcriptional control)[34,96]. Light-based actuation of gene expression patterning has been especially useful in 2D culture or optically transparent settings. However, the inherently poor penetration of light in densely populated tissues[97], long exposure times needed to activate molecular switches, and corresponding challenges in patterning light delivery have limited widespread adoption of light-based patterning of gene expression in 3D settings[98].

We hypothesized that we could overcome these challenges by exploiting more penetrant forms of energy to drive gene patterning. In particular, mild heating is an attractive option for 3D patterning across length scales, as heat can be targeted locally and penetrate tissues at depth. Furthermore, heat can diffuse through tissues to establish thermal gradients in predictable and controllable patterns that are dictated by established rules of heat transfer[99]. Last, advances in molecular engineering have led to proliferation of thermal molecular bioswitches to regulate gene expression[67,100], with mammalian systems activating in the mild hyperthermia range (~38° to 45°C). Heat transfer has a long industrial history, as heat is often added, removed, or moved between processes using heat exchangers, which transfer heat between fluidic networks. Recently, heat exchanger fabrication has undergone a radical shift due to developments in advanced manufacturing (e.g., 3D printing). Predating its history in industry, biological organisms have also long used heat exchanger design principles for thermoregulation. We reasoned that instead of building heat exchangers from hard materials, developing methods to build heat exchangers in materials compatible with living cells could facilitate volumetric heat patterning in artificial tissues.

5.2 Materials & Methods

5.2.1 *Cell culture*

HEK293T cells were maintained in Dulbecco's modified Eagle's medium (DMEM; Corning, NY, USA) supplemented with 10% (v/v) fetal bovine serum (FBS; Gibco) and 1% (v/v) penicillin-streptomycin (GE Healthcare Life Sciences, WA, USA).

5.2.2 *Construction of heat-sensitive reporter gene cells*

A vector containing a 476-bp version of the human HSPA6 promoter driving expression of fLuc reporter gene (gift of R. Schez Shouval from the Weizmann Institute of Science) was packaged into lentivirus using helper plasmids pMDLg/pRRE (Addgene no. 12251), pMD2.G (Addgene no. 12259), and pRSV-Rev (Addgene no. 12253) by cotransfection into HEK293T cells. Crude viral particles were harvested after 48 hours of transfection. For viral transduction, crude lentivirus was diluted 1:20 in DMEM containing polybrene (6 μg/ml; Invitrogen), added to competent HEK293T cells in six-well tissue culture plates, and incubated overnight (Corning). The next day, virus-containing media was removed and replaced with fresh DMEM containing 10% FBS. After transduction, cells were heat-activated (see below) and flow-sorted to obtain a pure cell population.

5.2.3 *Cell encapsulation and printing of cell-laden hydrogels*

Cultured HEK293T cells were detached from tissue culture plates with 0.25% trypsin solution (Corning), counted, centrifuged at 1000 rpm for 5 min, and resuspended in liquid prepolymer (7.5 wt % 6 K PEGDA, 7.5 wt % GelMA, 17 mM LAP, and 1.591 mM tartrazine). For characterization of heat transfer with respect to cell density, cells were encapsulated in prepolymer mixtures at final densities from 0 to 24×10^6 cells ml^{-1} before printing. For HEK293T expression studies, cells were encapsulated at a final density of 6 × 106 cells ml^{-1}. Printing was performed as previously described under DLP light intensities ranging from 17 to 24.5 mW cm^{-2}, with bottom layer exposure times from 30 to 35 s and remaining layer exposure times from 12 to 17.5 s. Upon print completion, fabricated hydrogels were removed from the platform with a sterile razor blade and allowed to swell in cell culture media. Hydrogels were

changed to fresh media 15 min after swelling and allowed to incubate overnight. Media was replaced the following morning.

We tested the viability of both HEK293T following 3D printing by incubating cell-laden hydrogels with Live/Dead viability/cytotoxicity kit reagents (Life Technologies, Carlsbad, CA) according to manufacturer's instructions. Fluorescence imaging was performed on a Nikon Eclipse Ti inverted epifluorescent microscope, and images were quantified using ImageJ's built-in particle analyzer tool [National Institutes of Health, Bethesda, Maryland].

5.2.4 *Heat treatment*

To activate transgene expression under the HSPA6 promoter, engineered HEK293T cells were exposed to varying levels of hyperthermia in 2D and 3D. For 2D heat treatment studies, cells were seeded at 8×10^4 cells/cm^2 in tissue culture plates 1 day before heat treatment. The next day, tissue culture plates were exposed to indicated heat treatments in thermostatically controlled cell culture incubators. Temperature was verified with a secondary method by a thermocouple placed inside the incubator. Upon completion of heat treatment, cells were returned to a 37°C environment and sorted or analyzed at later time points.

For the luminescent transient studies, cells were lysed in TE buffer [100 mM tris and 4 mM EDTA (pH 7.5)] and stored at 4°C until imaging. For the pulsed activation studies, cells received two heat shocks as described previously at days 0 and 3. Luminescence was quantified across days 1 to 4 and normalized to cell counts from tissue culture plates that were processed in parallel according to each experimental temperature.

For 3D heat shock studies, cells were encapsulated and printed in 3D perfusable hydrogels 1 day before heating. 3D hydrogels were then heat-perfused in a room temperature environment. Hydrogel temperature was monitored continuously with the infrared camera, and

small adjustments to heater power were made as necessary to maintain a stable temperature profile. During perfused heating, outlet medium was continuously discarded. Upon completion of perfused heating, hydrogels were dismounted from the perfusion chips and returned to a cell culture incubator.

5.2.5 *Bioluminescent imaging*

To visualize the magnitude and spatial localization of heat-induced luciferase expression, bioluminescence imaging was performed on heated cells and hydrogels using the in vivo imaging system (IVIS) Spectrum imaging system (PerkinElmer, Waltham, MA). Immediately before bioluminescence imaging, cell culture media was changed to media containing d-luciferin (0.15 mg/ml; PerkinElmer), and images were taken every 2 min until a bioluminescent maximum was reached. Images were analyzed using Living Image software (PerkinElmer). Luminescent imaging was performed from a “top-down” view (perspective orthogonal to hydrogel channel axis) for most studies. For cross-sectional images, hydrogels were manually sliced, incubated in luciferin containing media and imaged under cross-section view (perspective parallel to hydrogel channel axis).

5.2.6 *Pixel-to-pixel temperature-to-expression correlation*

Data for the expression versus temperature plot was obtained by aligning thermal and bioluminescent images using MATLAB. To align the images, four reference points corresponding to the corners of the hydrogel were manually selected on both thermal and bioluminescence images. Then, an orthogonal transformation was performed on each image to align the corners of the hydrogel, after which the areas outside the selection were cropped. Pixel values from each image were then plotted against each other to produce the expression versus temperature plot.

5.2.7 *Statistics*

Data in graphs are expressed as the SE or SEM ± SD, as denoted in figure legends. Statistical significance was determined using two-tailed Student's t test for two-way comparisons or one-way ANOVA or two-way ANOVA followed by Dunnett's, Sidak's, or Tukey's multiple comparison test.

5.3 RESULTS

5.3.1 *Generation and characterization of heat inducible cells*

We aimed to genetically engineer heat-inducible cells that activate gene expression upon exposure to mild hyperthermia. To do this, we implemented a temperature-responsive gene switch-based on the human heat shock protein 6A (HSPA6) promoter, which exhibits a low level of basal activity and a high degree of up-regulation in response to mild heating[101]. This promoter activates heat regulated transcription through consensus pentanucleotide sequences (5′-NGAAN-3′) called heat shock elements, which are binding sites for heat shock transcription factors[101]. We transduced human embryonic kidney (HEK) 293T cells with a lentiviral construct in which a 476–base pair (bp) region of the HSPA6 promoter containing eight canonical heat shock elements was placed upstream of a firefly luciferase (fLuc) reporter gene (**Figure 5.1**).

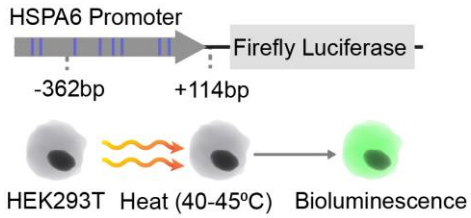

Figure 5.1. Schematic of heat-inducible gene expression in HEK293T: HEK293T cells are designed with a modified version of the human HSPA6 promoter containing 8 heat shock elements to activate expression of firefly luminescence in response to heat

Initial characterization of temperature-sensitive promoter activity in engineered cells in 2D tissue culture demonstrated a temperature-dose dependent up-regulation of luciferase activity in the range of mild hyperthermia (**Figure 5.2 A**). Statistically significant up-regulation was observed in heated cells compared to nonheated controls after hyperthermia for 30 min at 45°C or 60 min from 43° to 45°C, while peak bioluminescence occurred after 60 min at 44°C (292 ± 26-fold increase in bioluminescence relative to 37°C controls). We observed that our highest heat exposure (45°C for 60 min) led to a tradeoff between bioluminescence and cell integrity, as indicated by reduced cell metabolic activity and substrate detachment (**Figure 5.2 B**). These findings suggested that fine control of heat would be needed for thermofluidics to be useful in cellularized applications. Together, these studies demonstrate engineering of human cells with a heat-sensitive gene switch and identification of a tight window of thermal exposure parameters that both differentially up-regulate gene bioluminescence and maintain cell integrity.

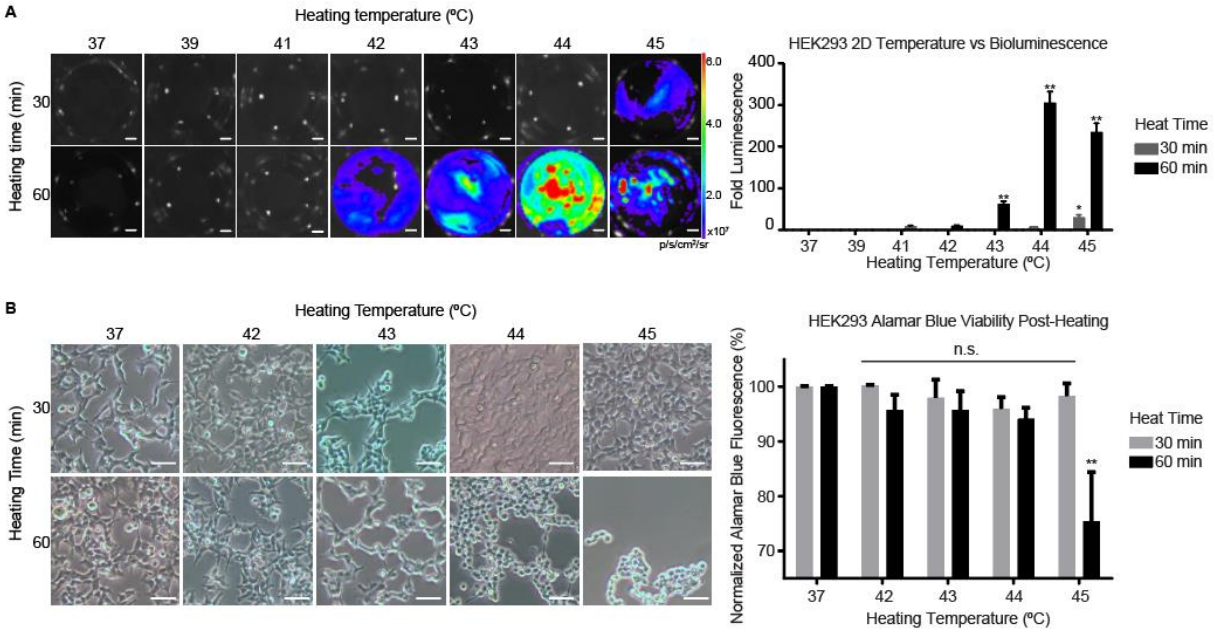

Figure 5.2. Thermal windows for heat induced upregulation of reporter genes in 2D cultured cells. (A) HEK293T cells transduced with human heat shock promoter 6a driving firefly luciferase exhibit a temperature dose-dependent upregulation of luciferase in 2D culture, as shown in representative luminescent images of differentially heated culture wells (left) and quantification of fold change in luminescence over 37ºC control (right, scale bars = 5 mm; n=3, data are mean fold luminescence ± standard error, *$p < 0.05$, **$p < 0.01$ by two-way ANOVA followed by Dunnett's multiple comparisons test). **(B)** Characterization of thermal dosage effect on cell viability in 2D and 3D. HEK293T cells cultured on tissue culture plastic demonstrated typical morphology upon exposure to 37-43ºC, became rounded upon exposure to 44ºC, and began to detach upon exposure to 45ºC after 60 minutes (left, scale bars = 50 µm). A significant decrease in cell reducing potential was observed after 60 min of heating at 45ºC but not at other temperatures (Alamar blue assay; fluorescence normalized to 37ºC condition; n = 3, data are

mean fluorescence percentage ± standard error, non-significant, n.s., **p < 0.01 by two-way ANOVA followed by Dunnett's multiple comparisons test.

We therefore rigorously characterized the effect of heating on HEK293T cells embedded in the hydrogel formulation used for our thermofluidic studies. Similar to 2D studies, cell viability fell significantly only after exposure to our highest temperature, 45°C (**Figure 5.3**).

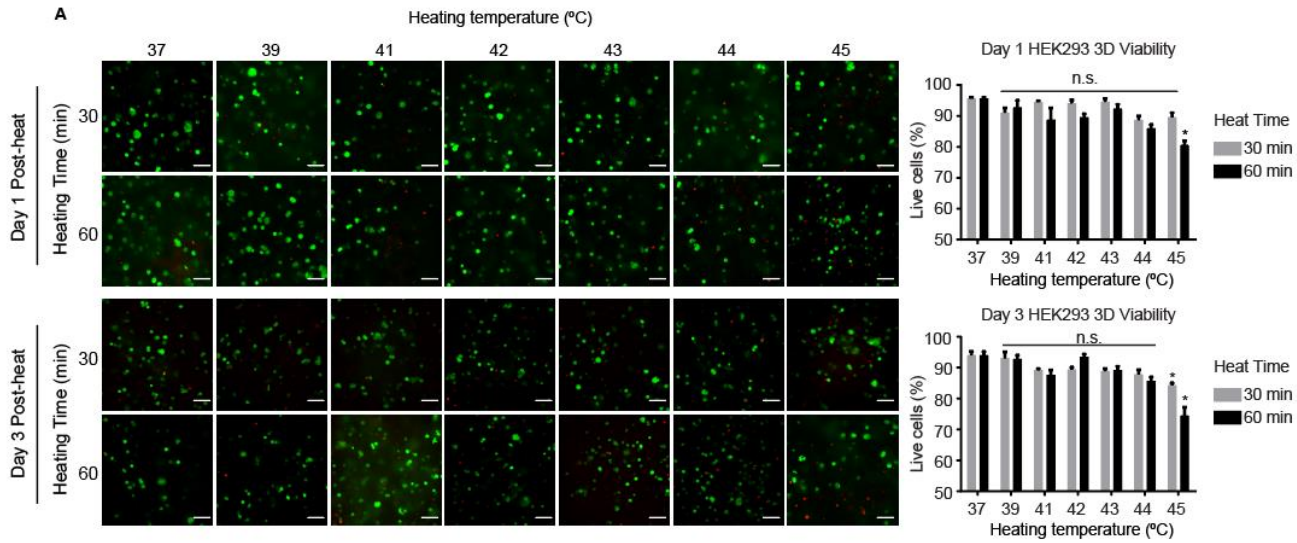

Figure 5.3 Thermal dosage effect on cell viability in 3D tissues. HEK293T cells printed in 3D hydrogels and exposed to the same hyperthermic conditions as in A show a similar viability trend as shown in representative Calcein/Ethidium Homodimer (Live/Dead) staining images. A significant decrease in viability is seen in hydrogels exposed to 45ºC for 60 minutes at 1 and 3 days post-heating and at 45ºC for 30 minutes 3 days post-heating but not at other temperature-time conditions (n=5, data are mean percentage ± standard error, non-significant, n.s., *p<0.05 by two-way ANOVA followed by Dunnett's multiple comparisons test).

Finally, we characterized both the kinetics heat-induced expression and robustness in response to pulsatility. For kinetic characterization, bioluminescent signal was first detected 8 hours after heat shock, peaked at 16 hours (110 ± 30-fold increase), and fell back to baseline by 2 days (**Figure 5.4 A**). Administration of a second heat shock stimulus 3 days later reinduced bioluminescent signal (**Figure 5.4 B**). Thus, gene activation with this promoter system is transient but can be reactivated with pulsing.

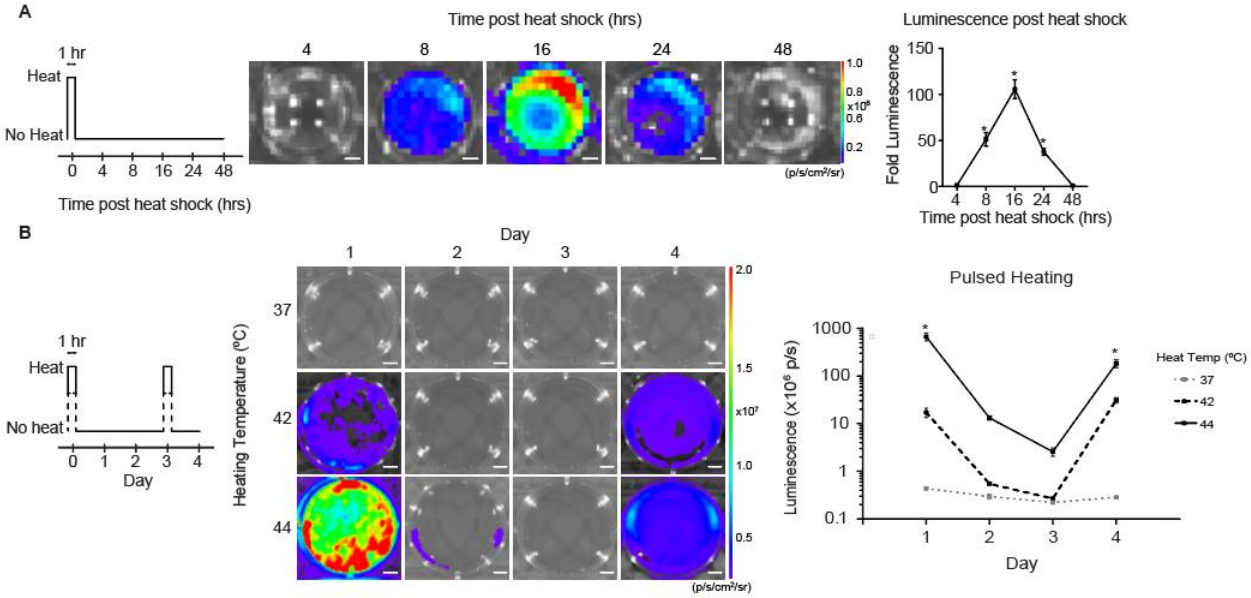

Figure 5.4. Kinetics and pulsatility of heat-inducible expression. **(A)** Heat inducible HEK293T cells were heat shocked for 1 hour at 44ºC and luminescence was quantified at various time points between 4 and 48 hours after heat shock induction showing significant signal compared t between 8 - 24 hours and peaking at 16 hours (scale bars = 1 mm; n = 9, data are mean fold luminescence ± standard error, *p<0.05 by one-way ANOVA followed by Dunnett's multiple comparison test). **(B)** Heat inducible HEK293T cells were heat shocked twice, at 42ºC or 44ºC, over the course of four days at days 0 and 3 with luminescence measured each day. Significant increases in luminescence were observed at 44ºC compared to 37ºC controls at days 1

and 4 (scale bars = 5 mm; n = 6, data are mean luminescence error bars ± standard error, *p<0.05 by two-way ANOVA followed by Tukey's multiple comparison test).

5.3.2 *3D Thermofluidic characterization of heat-inducible cells*

We sought to determine whether thermofluidic heating could be used to induce gene expression in heat-inducible cells encased within 3D artificial tissues (**Figure 5.5 A**). To do this, we encapsulated heat-inducible cells in the bulk of bioprinted constructs that contained a single perfusable channel (**Figure 5.5 A**). Since tissue constructs were printed from biocompatible materials without ultraviolet light cross-linking, most cells remained viable upon encapsulation (**Figure 5.5 B**).

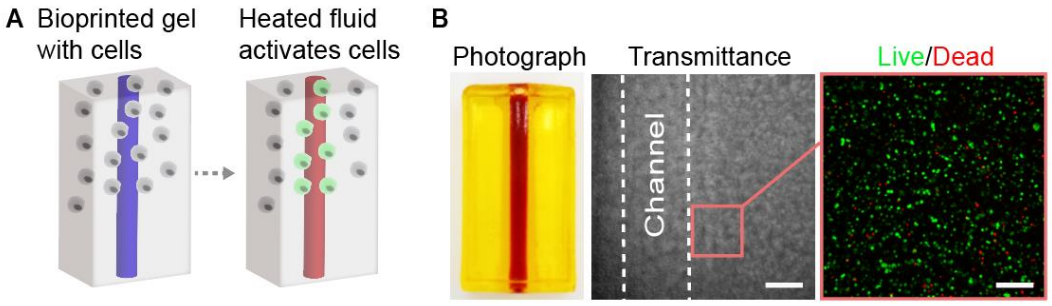

Figure 5.5. Thermofluidic activation of encapsulated cells: **(A)** Schematic of thermofluidic encapsulation and activation. **(B)** Single-channel tissue used for 3D heat activation (left). Scale bar, 3 mm. Transmittance image of cellularized hydrogel after printing (middle). Scale bar, 500 µm. HEK293T cells in bioprinted tissues stained with calcein-AM ("live," green) and ethidium homodimer ("dead," red; right). Scale bars, 200 µm

To determine whether our heat-inducible cells could be activated using thermofluidics, we perfused channels at 0.5 ml min^{-1} using thermal exposure parameters identified in 2D culture

(**Figure 5.6 A**). Similar to 2D, we observed that thermal dose-dependent luciferase up-regulation (**Figure 5.6 C-E**) was statistically significant after 30 min of heating to a target hydrogel temperature of 44°C or after 60 min of heating to temperatures of 43° and 44°C by whole-gel bioluminescent output (71 ± 22-fold and 169 ± 44-fold increase relative to controls, respectively; **(Figure 5.6 C-E**). Similar to 2D, we observed that thermal dose-dependent luciferase up-regulation (Fig. 3, F to J) was statistically significant after 30 min of heating to a target hydrogel temperature of 44°C or after 60 min of heating to temperatures of 43° and 44°C by whole-gel bioluminescent output (71 ± 22-fold and 169 ± 44-fold increase relative to controls, respectively; (**Figure 5.6 D-F**).

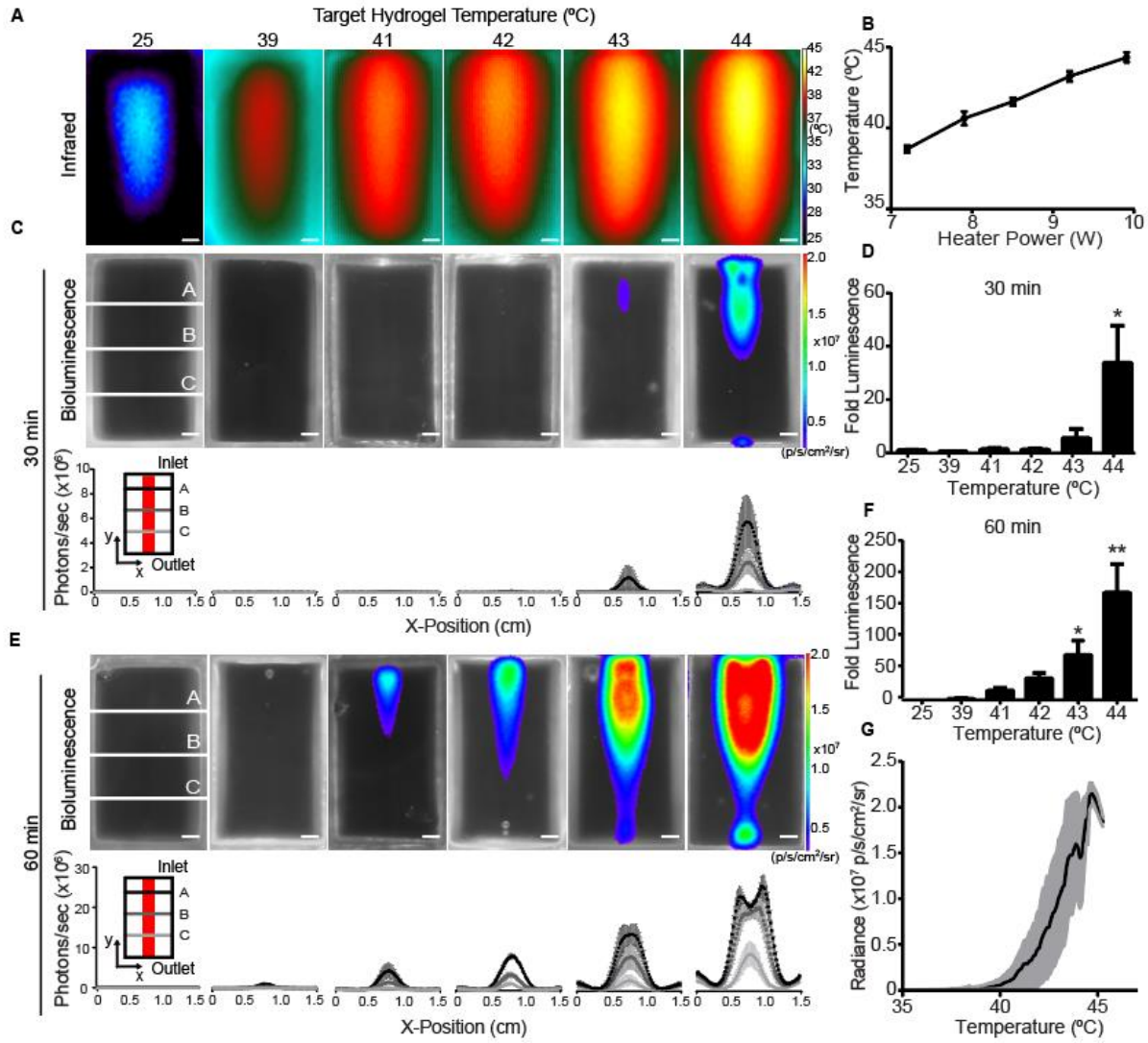

Figure 5.6. Fluidic heating induces gene expression in 3D artificial tissues: (A) Representative infrared images of thermofluidic perfusion in single-channel hydrogels. Scale bars, 2 mm. **(B)** Hydrogel temperatures are tuned by changing heater power at constant flow rate (n = 3, mean temperature ± standard error). **(C)** Representative bioluminescence images of hydrogels (top; scale bars, 2 mm) and intensity traces at three positions (A to C) across the width (x) of the hydrogel after 30 min of perfused heating. **(D)** Fold change in bioluminescence after 30 min of heating relative to 25°C controls. **(E)** Representative bioluminescence images of hydrogels (top; scale bars, 2 mm) and intensity traces after 60 min of perfused heating (bottom;

scale bars, 2 mm). **(F)** Fold change in bioluminescence after 60 min of heating demonstrates a temperature-dependent dosage response in gene expression [(D and F); n = 3, mean fold luminescence ± standard error; *P < 0.05 and **P < 0.01 by one-way ANOVA followed by Dunnett's multiple comparison test]. **(G)** Temperature-expression response curve (black) shows mean bioluminescent radiance across temperature; shaded regions (gray) indicate ± SD. N = 3.

To more finely characterize how bioluminescent intensity correlates with temperature, infrared and bioluminescence images were overlaid to map individual pixels and generate temperature-bioluminescence response curves. The shape of temperature-response curves appeared similar in shape across various target temperatures (**Figure 5.7**). Similar to whole-gel analyses, greater target temperatures generated the most robust activation (**Figure 5.6** and **Figure 5.7**)

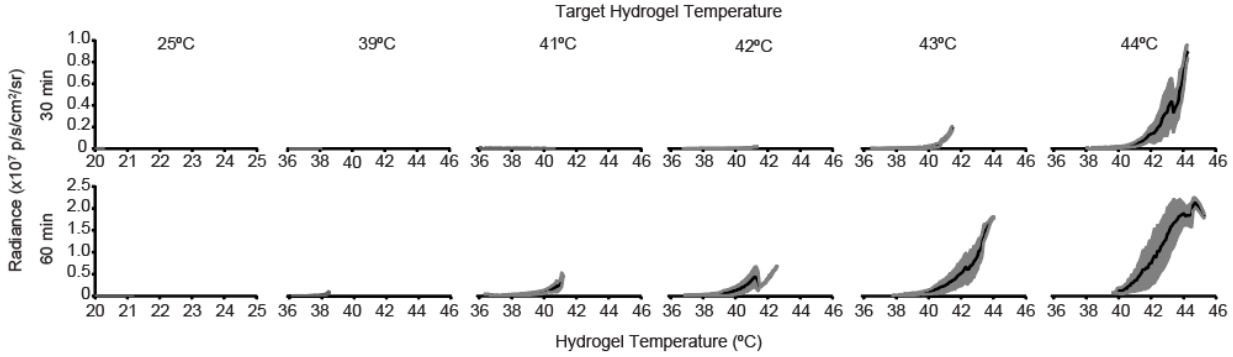

Figure 5.7. Temperature expression relationship in differentially heated hydrogels. Response curves from each hydrogel temperature condition. Analysis shows in 60 min heating charts, bioluminescence is activated beginning at 40ºC, increases nonlinearly and peaks at ~44ºC. Above 44ºC bioluminescence begins to drop off due to thermal stress. Data are mean radiance (black curve) ± standard deviation (shaded area).

Last, multi-perspective imaging and bioluminescence quantification of single-channel perfused hydrogels from both "top-down" and "cross-sectional" perspectives demonstrated that reporter gene activation had a 3D radial gradient topology around each channel (**Figure 5.8**). Together, these results illustrate that thermofluidics can be used to activate varying levels of gene expression in 3D artificial tissues.

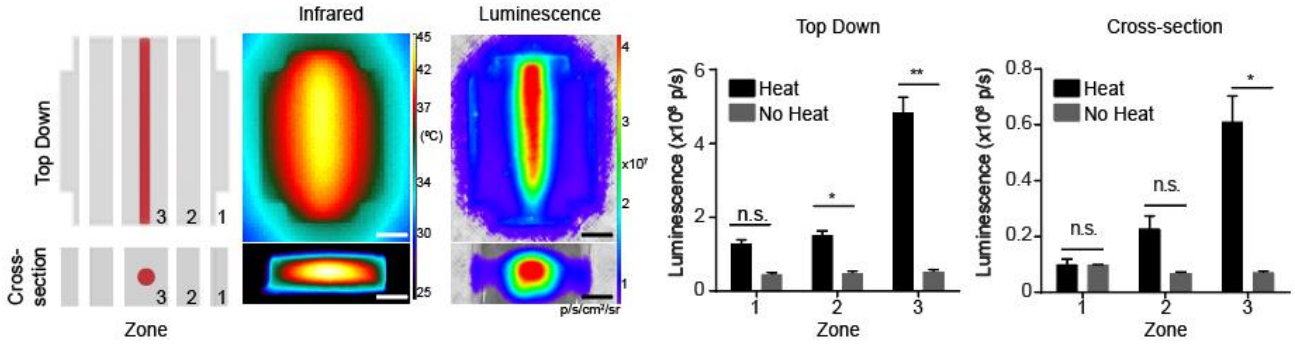

Figure 5.8. Multi-perspective bioluminescent imaging of thermofluidically heated gels. Bioluminescence from single channel heated gels was quantified by dividing each gel into 3 zones and viewing the gels from 'Top-down' and 'Cross-section' perspectives (scale bars = 2 mm). Luminescence quantification under both perspectives shows peak expression occurs nearest the channel and decays radially outwards (n=5, data are mean luminescence ± standard error, non-significant, n.s., *p<0.05, **p<0.01 by two-way ANOVA followed by Sidak's multiple comparisons test).

5.3.3 *Heat exchangers for spatial and dynamic control of gene expression patterning*

Spatial patterns of gene expression within native tissues vary widely in magnitude, scale, and spatial complexity. While we achieved variation in magnitude in our signal-channel studies, the expression profile geometry across the hydrogel remained similar at various perfusion

temperatures. This raised the question of how to design heat delivery schemes that enable more spatially complex expression patterns across the hydrogel. Our thermal characterization revealed flow rate as one parameter that we could use but changing flow rate alone imparted only subtle differences to the spatial thermal profile. To identify a more perturbative and user-defined means of affecting heat distribution across the hydrogel, we turned to industrial heat transfer applications, in which heat exchangers are optimized to transfer heat between fluids by controlling parameters such as channel placement and flow pattern.

We mimicked a double pipe heat exchanger design within cellularized hydrogels by printing two channels at varying distances from one another (**Figure 5.9, narrow versus wide**). We then perfused hydrogels under different conditions for flow direction (concurrent versus countercurrent) and fluid temperature [hot (44°C) versus cold (25°C)]. Similar to our single-channel characterization, double-channel tissues showed close matching between thermal and bioluminescence profiles. Concurrent flow in narrow spaced channels created elongated spatial plateaus of heat and bioluminescence between the channels. Conversely, widely spaced hot channels generated mirror imaged thermal and bioluminescent profiles, with distinct spatial separation between channels. Countercurrent flow patterns generated parallelogrammic thermal and bioluminescent profiles in both channel spacings. Substituting a hot channel for a cold channel attenuated bioluminescence in a manner that depended on channel spacing (**Figure 5.9**).

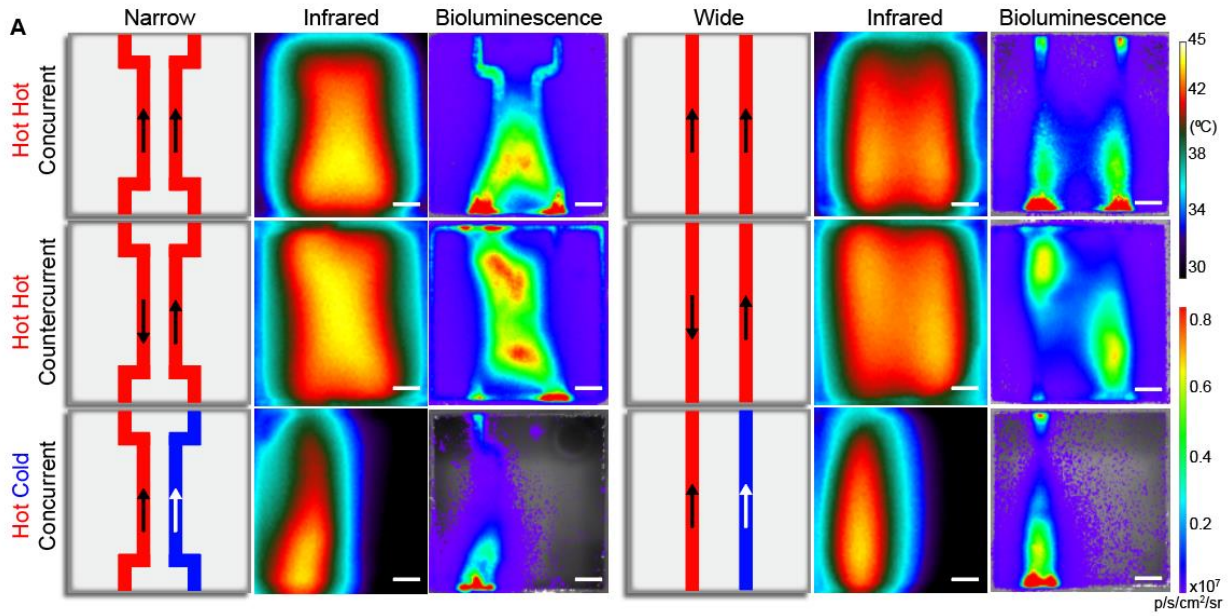

Figure 5.9. Heated perfusion heat exchanger network architectures generates variation in spatial expression patterns: Heat exchanger inspired designs for various flow directions, fluid temperatures, and channel architectures (schematics; left and center). Representative thermal (middle) and bioluminescent (right) images demonstrate spatial tunability of thermal and gene expression patterning. Scale bars, 5 mm.

As biological gene expression patterns are transient and fluctuating, we next tested whether thermofluidics could dynamically localize regions of gene expression over time. To do this, we printed clock inspired constructs, in which four separate inlets converged on a circular channel (**Figure 5.10 A, top**). We then perfused heated fluid through each inlet over four consecutive days (**Figure 5.10 A, bottom**) and imaged tissues for bioluminescence. Bioluminescent images demonstrated statistically significant luciferase up-regulation for regions surrounding heated inlets compared to nonheated inlet regions on all 4 days (**Figure 5.10 B)** Together, our results illustrate that by exploiting heat transfer design principles, thermofluidics

enables user-defined spatial and dynamic patterning of mesoscale gene expression patterns in 3D artificial tissues.

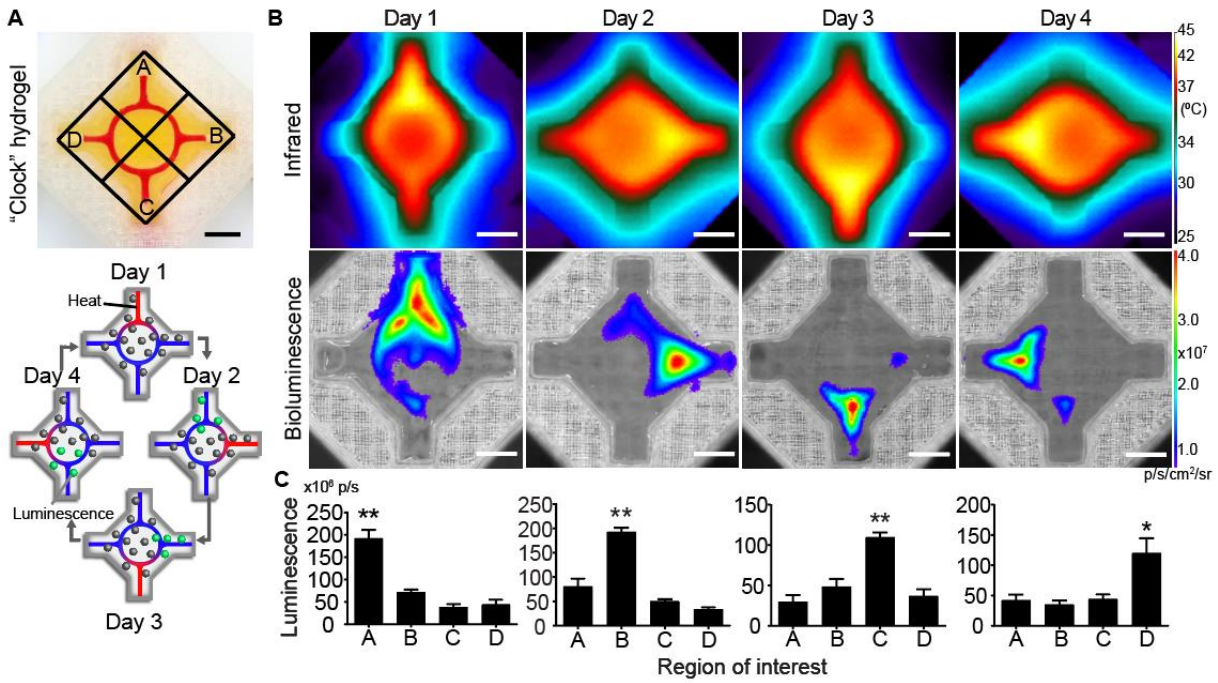

Figure 5.10. Heated perfusion of clock inspired construct dynamically localizes gene expression over space and time: (A) Photographic image of four-armed clock-inspired hydrogel used for dynamic activation (top; channel filled with red dye). Each inlet is assigned to a local region (A to D). Schematic shows the spatial and dynamic heating pattern for the 4-day study (bottom). **(B)** Representative infrared (top) and bioluminescence expression (bottom) images for dynamic hydrogel activation at each day during the time course. **(C)** Quantification of local bioluminescent signals from regions of interest corresponding to each day of heating. Across all 4 days, regions corresponding to perfused arms had higher bioluminescent signals than nonperfused arms (n = 5, data are mean luminescence ± standard error; *P < 0.05 and **P < 0.01 by one-way ANOVA followed by Tukey's post hoc test).

5.4 DISCUSSION & CONCLUSIONS

In this chapter, we demonstrate that thermal patterning via bioprinted fluidics can directly pattern gene expression in 3D artificial tissues. A key advantage of the HEAT method is that it leverages the recent explosion in accessible additive manufacturing tools[12,74] by using open-source bioprinting methods that are readily available to the broader community. Furthermore, the entire patterned network is stimulated nearly simultaneously (as opposed to sequentially by time-intensive rastering), and this parallel stimulation can be sustained for exposure times required to trigger gene expression. Together, the sheer rapidity and highly parallel nature of this process enable spatial and dynamic genetic patterning at length scales and depths not previously possible in 3D artificial tissues.

Most previous methods to elicit cellular signaling in artificial tissues have focused on tethering extracellular cues to hydrogels[102,103]. Innovations in stimuli-responsive or 'smart' biomaterials enabled activation of such chemistries by exogenous physical stimuli, such as light, to control the spatial position and timing of extracellular cues[104,105]. Although useful, such materials-focused methods are unlikely to provide complete control even in fully defined starting environments because cells rapidly remodel their microenvironments[106]. Moreover, such technologies offer an imprecise means to control downstream transcription because many, often unknown, intermediary steps modify intracellular signal transduction prior to gene activation. Our thermofluidic approach provides a complementary new technology to such methods that target extracellular signals by facilitating spatiotemporal control at the intracellular genetic level.

Chapter 6. SLATE & HEAT FOR ARTIFICIAL LIVER TISSUE ENGINEERING

6.1 INTRODUCTION

The global health burden imposed by liver disease is on an upward trend, in 2000 the global death share from end-stage liver disease was 3%, by 2015 it was 3.5%, accounting for 2 million deaths globally[107,108]. Organ transplant remains the only curative treatment, but the demand for transplantable organs far exceeds the supply[109]. Artificially engineered hepatic tissues have shown promise as a solution to the organ shortage but these technologies are still developing[110]. To reach maturation, more efficient approaches to engineer biomaterials, organize tissue architecture, and replicate the phenotype in native hepatic tissues are required. Among these approaches, 3D bioprinting is unique in its ability to automate, scale-up and distribute tissue fabrication processes across several locations.

Beyond practical benefits, studies on 3D bioprinted hepatic tissues are validating the capacity of this technology to preserve and enable biological function. For example, the ability to compartmentalize structures for organized assembly of hepatocytes and endothelial cells that leads to improved hepatic function and vascularization; first being demonstrated in manually fabricated hydrogels[111], has been replicated in 3D bioprinted constructs[112,113]. Similarly, 3D bioprinting enables facile creation of perfusable channel systems composing multiple biomaterials, this capability enhances the achievable complexity of engineered hepatic tissues[114,115].

Further improvements towards biomimicry can be achieved by combing 3D structural patterning physicochemical stimuli patterning in engineered biosystems. For example, a hallmark of liver physiology is liver zonation, a process in which hepatocytes become specialized to perform specific metabolic functions based on their position within the liver lobule[116]. In the body, this

specialization occurs as hepatocytes, distributed along the portal-central vein axis, are exposed to oxygen, nutrient, hormone, metabolite, and morphogen gradients (**Figure 6.1**)[116]. Hepatocytes exposed to chemical and morphogen gradients in artificial systems can be induced towards a zonal phenotype. For example, McCarty et al.[117] using microfluidically generated gradients of insulin and glucagon demonstrated *in vitro* zonation of isolated hepatocytes in 2D as evidenced by gradients in urea production, glycogen storage and cell viability in an acetaminophen toxicity assay. In their work, "Zone-3" hepatocytes which highly expressed CYP P450 drug metabolizing enzymes were significantly more susceptible to cell death upon exposure to acetaminophen than any other zone. An identical zonal pattern for acetaminophen toxicity was also observed by Ahn et al[118]. using HepaRG cells in a 3D agarose model, whereas non-zonated models did not display spatial differences in viability. These findings suggest that establishing a zonal phenotype is an important step to creating more biomimetic engineered hepatic tissues on the way to artificial livers.

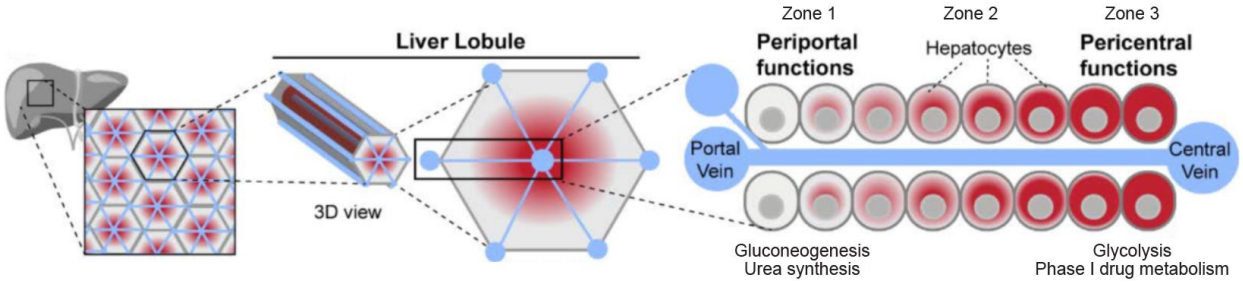

Figure 6.1. Schematic of hepatic zonation: Hepatocytes are classified as belonging to zones 1, 2, or 3. Zone 1 corresponds to the space surrounding the portal vein where hepatocytes are specialized for gluconeogenesis and urea synthesis. Zone 3 corresponds to the space surrounding the central vein where hepatocytes are adapted for drug metabolism. Zone 2 hepatocytes display an intermediate phenotype.

At the molecular level, liver zonation is regulated by a gradient in Wnt/β-catenin signaling. Higher Wnt activity associated with a zone 3 (pericentral) and lower Wnt activity characteristic of a zone 1 (periportal) phenotype[119]. Accordingly, genetic perturbation of this pathway is being explored to generate functional zonated tissue. Wahlicht et al[120]. recently reported a system in which they re-engineered hepatocytes with a doxycycline-inducible cassette for overexpression of the β-catenin transcription factor. Doxycycline mediated activation of Wnt signaling established a pericentral phenotype as indicated by a shift in gene expression, increase in autophagy, and higher susceptibility to hepatitis C infection. However, hepatocytes were only characterized on a binary basis (according to +/- doxycycline), thus valuable information on how intermediate levels of Wnt signaling impact hepatic function was not available.

In this work, we explore state-of-the-art hepatic tissue engineering from multiple, complementary directions. First, we examine the potential of 3D bioprinting systems to build multi-material liver tissues that enhance hepatocyte survival and function after implantation using SLATE fabrication. Then, we explore the potential of combining remote fields with genetic rewiring to fabricate zonated liver tissues using our HEAT system. Together, these technological innovations demonstrate the emerging strategies towards therapeutic engineered hepatic tissue.

6.2 MATERIALS AND METHODS

6.2.1 *Cell Culture*

Primary human umbilical endothelial cells (HUVECs; Lonza; passages 4 to 7) were maintained on dishes in EGM-2 (Lonza). Normal human dermal fibroblasts (NHDFs; Lonza; passages 4 to 9) were cultured in DMEM with 10% (v/v) FBS (source) and 1%(v/v) penicillin-streptomycin. Differentiated HepaRG cells (Fisher Scientific) were maintained at confluence in

six-well plates at a density of 2 × 106 cells per well in Williams E media (Lonza, MD, USA) supplemented with 5× HepaRG Thaw, Plate & General Purpose Medium Supplement (Fisher), and 1% (v/v) Glutamax (Fisher).

6.2.2 *Rat Hepatocyte Isolation and Culture*

Rat primary hepatocytes were isolated as described previously[121] and maintained in highglucose DMEM containing 10% (vol/vol) fetal bovine serum (Gibco), 1% (v/v) ITS supplement (insulin, transferrin, sodium selenite; BD Biosciences), 7 ng/mL glucagon (Sigma), 0.04 µg/mL dexamethasone (Sigma) and 1% penicillin-streptomycin (pen-strep, Invitrogen).

6.2.3 *Lentiviral transduction*

For hydrogel carrier studies, to enable non-invasive imaging of hepatocyte function, primary hepatocytes were transduced with a lentiviral vector expressing firefly luciferase under the albumin promoter (pTRIP.Alb.IVSb.IRES. tagRFP-DEST, provided through a Materials Transfer Agreement with Charles Rice, The Rockefeller University) as previously described[122]. For viral transduction, concentrated virus was diluted 1:5 in hepatocyte medium containing HEPES 16buffer (20 mM; Gibco) and polybrene (4 µg/ml; Sigma) in 6-well ultra-low attachment plates (Corning) for 6 hrs. Concentrated virus was diluted 1:5 in hepatocyte medium containing HEPES 16buffer (20 mM; Gibco) and polybrene (4 µg/ml; Sigma) in 6-well ultra-low attachment plates (Corning) for 6 hrs.

For heat-inducible Wnt studies, Lentiviral constructs in which the HSPA6 promoter drives a Wnt family gene were subcloned using Gibson assembly by the UW BioFab facility. Human beta-catenin pcDNA3 was a gift from Eric Fearon (Addgene plasmid # 16828)[123]. Active Wnt2-V5 was a gift from Xi He (Addgene plasmid # 43809)[124]. RSPO1 was subcloned using a

cDNA clone plasmid. (Sino Biological, Beijing, China). All plasmids contained a downstream cassette in which a constitutive promoter (spleen focus-forming virus, SFFV) drives the reporter gene mCherry (gift from Dr. Gabriel A. Kwong, Georgia Institute of Technology). Lentivirus was generated by co-transfection of HEK293Ts or HepaRGs with HSPA6→Wnt transfer plasmids with 3rd generation packaging plasmids (pMDLg/pRRE, pMD2.G, pRSV-REV) in DMEM supplemented with 0.3% Xtreme Gene Mix (Sigma). Crude virus was harvested starting the day after initial transfection for four consecutive days. For viral transduction, HEK293Ts at 70% confluency and HepaRGs at 100% confluency were treated with crude virus containing polybrene (8 µg/mL, Sigma) for 24 hours. Five days following viral transduction, mCherry positive HEK293Ts sorted from the bulk population by flow cytometry at the UW Flow analysis facility. HepaRGs were not sorted by flow cytometry. mCherry expression in positive HEK293T cell populations was performed using RT-qPCR.

6.2.4 *Fabrication of Engineered Hepatic Tissues*

For hydrogel carrier studies engineered hepatic tissues were fabricated in a three-step process. First, hydrogel carriers were printed from either 30 wt% 6 kDa PEGDA, a mixture of 7.5:7.5 wt% 6 kDa PEGDA:GelMA, or a mixture of 3.25 wt% 3.4 kDa PEGDA + 10 wt% GelMA at 50 micron layer thickness. Gels were rinsed and incubated in PBS for 24 hrs prior to cell seeding. Second, to populate hepatic tissues with endothelial cell (EC) cords, HUVECs were suspended at a density of 10 million HUVECs/mL in neutralized liquid collagen (2.5 mg/mL) (Corning). HUVEC-collagen slurry was pipetted into open channels. Constructs were incubated in EGM-2 media for 4 hours to allow for cord formation. Third, to create hepatic aggregates, rat primary hepatocytes were plated in AggreWell micromolds (400µm square AggreWell

micromolds, Stem Cell Technologies) along with NHDFs at a 1:1 ratio and incubated overnight. Following EC cord formation, hepatic aggregates (100 hepatocytes and 100 dermal fibroblasts per aggregate) were suspended in either fibrin (10 mg/mL) or 5 wt% GelMA at a concentration of 45,000 aggregates/mL casting suspension and pipetted into the hepatic tissue infill space. For HEAT studies, HEK293Ts and HepaRGs for a given construct were encapsulated and heated in 3D hydrogels as described previously in the methods of Chapter 4.

6.2.5 *In Vivo implantation and imaging of Engineered Tissues*

All surgical procedures were conducted according to protocols approved by the University of Washington Animal Care and Use Committee. For hydrogel carrier studies, Female NCr nude mice aged 8-12 weeks old (Taconic; Fig. 4A-D) or male Fah-/- backcrossed to NOD, Rag1-/-, and Il2rg-null (FNRG) mice aged 30-40 weeks old (Yecuris) were anesthetized using isoflurane, and the engineered tissue constructs were sutured to the perigonadal fat pad. The incisions were closed aseptically, and the animals were administered buprenorphine (0.1 mg/ml) every 12 hours for 3 days after surgery. NTBC was withdrawn from the animals' drinking water immediately after tissue implantation and for 14 days after implantation. Prior to bioluminescence imaging, mice were injected intraperitoneally with 250 µL of D-luciferin (15 mg/mL; GoldBio) and imaged using the IVIS Spectrum In Vivo Imaging System (Xenogen) and Living Image software (Caliper Life Sciences) after 14 days of implantation.
For HEAT-modulated artificial tissues, artificial tissues were implanted subcutaneously on the ventral side of female NCr nude mice aged 8 to 12 weeks old (Taconic). Twenty-four hours after implantation, mice were anesthetized and injected with luciferin (15 mg/ml; PerkinElmer, Waltham, MA). Bioluminescence was then recorded via the IVIS Spectrum Imaging System (PerkinElmer). For 3D images, a custom 3D imaging unit developed by A. D. Klose and N.

Paragas[125] (InVivo Analytics, New York, NY) was used. Briefly, anesthetized mice were placed into body-fitting animal shuttles and secured into the custom 3D imaging unit that uses a mirror gantry for multiview bioluminescent imaging. Collected images were then compiled and overlaid onto a standard mouse skeleton for perspective.

6.2.6 *Spatial analysis of HEAT-modulated bioluminescence images*

Line profiles in the x-direction across the inlet, middle, and outlet of 2D IVIS projection images from artificial gels were generated using Living Systems software (PerkinElmer, Waltham, MA). The three line profiles (inlet, middle, and outlet) from each artificial tissue were then averaged together with the average line profiles from the other artificial gels within each respective group (experimental group, n = 5; positive control group, n = 3; negative control group, n = 3). The average line profile of each group was then plotted, and average radiance values from positions 0.75 cm from the center of the channel (denoted positions A and C) were then statistically compared to the average radiance value at the center of the channel (position B) within each group by one-way analysis of variance (ANOVA).

6.2.7 *Tissue Harvesting, Processing, Histology and Immunohistochemistry*

For hydrogel carrier studies animals were sacrificed at the termination of the experiment (10-14 days) following bioluminescence imaging. Tissues were harvested from the intraperitoneal space and fixed in 4% (v/v) paraformaldehyde for 48 hours at 4 ºC, incubated in OCT embedding medium (Fisher) for 24 hr at 4 ºC, flash-frozen in dry-ice ethanol slurry and sectioned using a cryostat (5 µm) for immunohistochemical analysis. For gross visualization of tissue, sections were stained with hematoxylin and eosin. For identification of primary rat hepatocytes, sections were first permeabilized with 0.1% Triton-X, blocked with 1.5% normal

donkey serum and immunostained with primary antibodies against cytokeratin-18 (rabbit, 1:100; Abcam) followed with species-appropriate secondary antibodies conjugated to (Alexa Fluor 594). To determine graft size, we used Adobe Photoshop to quantify the number of cytokeratin-18 positive pixels in each graft. For identification of mouse red blood cells, sections were permeabilized with 0.1% Triton-X, blocked with 1.5% normal donkey serum and immunostained with primary antibodies against Ter-119 (rat, 1:100; BD Pharmingen) and visualized with species appropriate secondary antibodies conjugated to Alexa Fluor 488. Images were obtained using a Nikon A1R confocal at the Garvey Imaging Lab in the Institute for Stem Cells and Regenerative Medicine (ISCRM) at the University of Washington.

For HEAT-modulated tissues, HSPA6→Wnt2/V5 gels were fixed in 4% paraformaldehyde 24 hours post-heating. For staining, samples are blocked overnight at room temperature in 1% BSA + 1% normal donkey serum + 0.1M tris + 0.3% Triton X-100 with agitation. After blocking, samples are incubated in Anti-V5 tag antibody (Abcam, ab27671) diluted 1:100 in fresh blocking buffer + 5% dimethyl sulfoxide for 24 hours at 37ºC and agitation. Samples are washed, then incubated in secondary antibody diluted 1:500 in fresh blocking buffer + 5% dimethyl sulfoxide overnight at 37ºC and agitation. After incubation samples are washed in PBS + 0.2% Triton X-100 + 0.5% 1-thioglycerol three times at room temperature and agitation, changing fresh buffer every 2 hours. To begin clearing, samples are incubated in Clearing Enhanced 3D (Ce3D)[126] solution at room temperature overnight with agitation protected from light. DAPI is diluted 1:500 in the Ce3D solution in order to counter stain for nuclei. To 3D image the cleared samples, the gels are placed on glass-bottom dishes and imaged overnight on an SP8 Resonant Scanning Confocal Microscope.

6.2.8 *Wnt upregulation in HEAT-induced constructs*

To quantify Wnt regulator levels in HEAT treated gels, HEK293Ts and HepaRGs for a given construct were encapsulated and heated in 3D hydrogels as previously described. 'No heat control' samples remained at 37ºC in tissue culture incubators until RNA isolation. 1 -48 hours following heat treatment, hydrogels were manually sliced into corresponding zones (1, 2, 3) and RNA was isolated using phenol-chloroform extraction[127]. cDNA was synthesized using the Superscript III First strand synthesis kit (ThermoFisher) and qPCR performed using iTaq Universal SYBR Green Supermix (Biorad, Hercules, CA on a 7900HT Real Time PCR system (Applied Biosystems, Waltham, MA). Primers for Wnt and housekeeping genes were designed and synthesized by Integrated DNA Technologies (Coraville, IA). Relative gene expression was normalized against the housekeeping gene 18s RNA calculated using the ΔΔCt method. Data are presented as the mean relative expression ± s.e.m. Data for HEK293T studies was normalized to relative expression of the Wnt target in 2D culture at 37ºC. Data for HEK293T mCherry expression was normalized to 18s RNA and compared to GAPDH (also normalized to 18s RNA) expression levels. Data for HepaRG studies was normalized by relative expression of the Wnt target or pericentral/periportal gene marker to 'No heat control' samples.

6.2.9 *Statistics*

Data in graphs are expressed as the SE or SEM ± SD, as denoted in figure legends. Statistical significance was determined using two-tailed Student's t test for two-way comparisons or one-way ANOVA or two-way ANOVA followed by Dunnett's, Sidak's, or Tukey's multiple comparison test.

6.3 RESULTS

6.3.1 *Functional characterization of 3D bioprinted hepatic hydrogel carriers*

We sought to establish the utility of SLATE for fabricating structurally complex and functional tissues for therapeutic transplantation. In particular, the liver is the largest solid organ in the human body, carrying out hundreds of essential tasks in a manner thought to be dependent on its structural topology. We created complex structural features in hydrogel within the expanded design space imparted by SLATE to assemble multi-material liver tissues. Bioprinted single-cell tissues and bioprinted hydrogel carriers containing hepatocyte aggregates were fabricated (**Figure 6.2 A-C**). The albumin promoter activity of tissue carriers loaded with aggregates was enhanced by more than a factor of 60 compared with that of implanted tissues containing single cells (**Figure 6.2 B,C**). Furthermore, upon gross examination of tissues after resection, hydrogel carrier tissues appeared to have more integration with host tissue and blood (**Figure 6.2 D**).

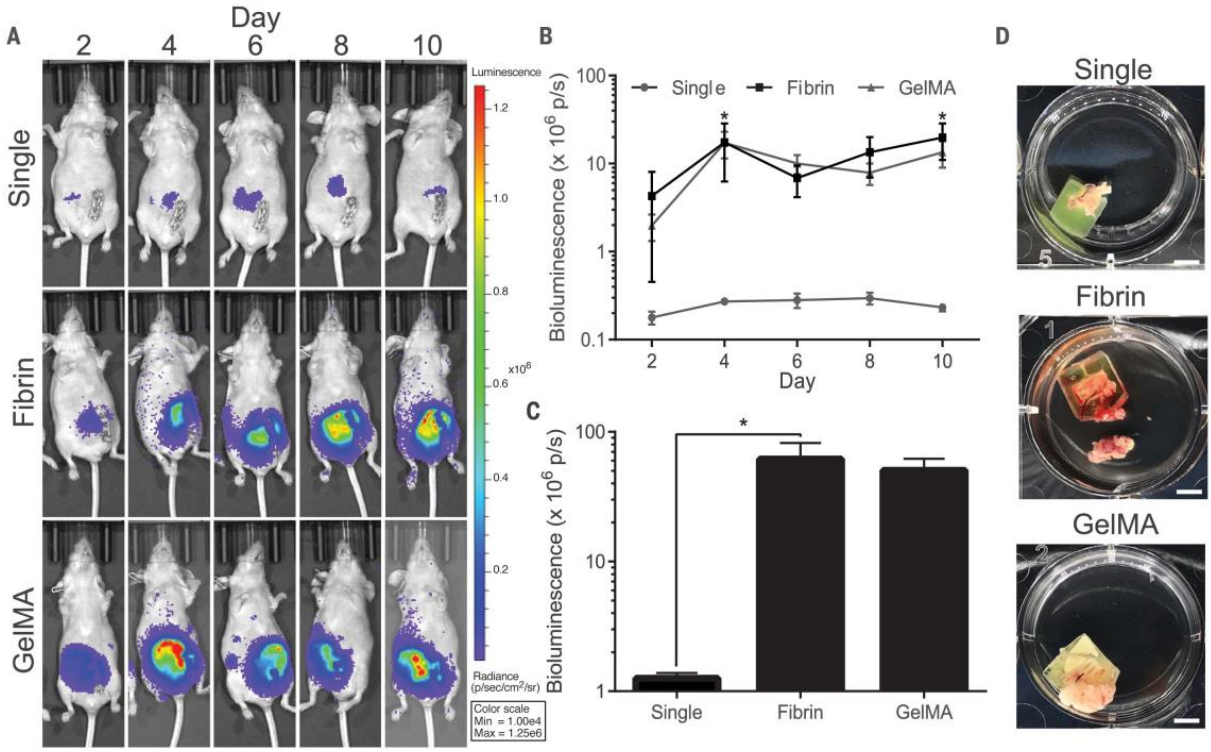

Figure 6.2. Engraftment of functional hepatic hydrogel carriers. (**A**) Albumin promoter activity was enhanced in hydrogel carriers containing hepatic aggregates after implantation in nude mice. Data from all time points for each condition are shown in (**B**) [N = 4, *P < 0.05 by two-way analysis of variance (ANOVA) followed by Tukey's post-hoc test]. Cumulative bioluminescence for each condition is shown in (**C**) (N = 4, *P < 0.05 by one-way ANOVA followed by Tukey's post-hoc test). Error bars indicate SEM. GelMA, gelatin methacrylate.

Despite the improved utility of hepatic aggregates over single cells, aggregate size puts substantial architectural limitations on 3D printing because aggregates are larger in size than our lowest voxel resolution (50 μm). To accommodate these design constraints, we built a more advanced carrier that can deliver hepatic aggregates within natural fibrin gel, has a vascular compartment that can be seeded with endothelial cells, and incorporates structural hydrogel anchors to physically, rather than chemically, retain the fibrin gel and facilitate remodeling

between the graft and host tissue (**Figure 6.3 A**). Microchannel networks were seeded with human umbilical vein endothelial cells (HUVECs) because our previous studies demonstrated that inclusion of endothelial cords improved tissue engraftment[128].

We then evaluated whether optimized bioengineered liver tissues would survive transplantation in a rodent model of chronic liver injury. After 14 days of engraftment in mice with chronic liver injury, hepatic hydrogel carriers exhibited albumin promoter activity indicative of surviving functional hepatocytes (**Figure 6.3 B**). Immunohistological characterization revealed the presence of hepatic aggregates adhered to printed hydrogel components that stained positively for the marker cytokeratin-18 (**Figure 6.3 B-C**). Further characterization through gross examination and higher magnification images of slides stained with hematoxylin and eosin (H&E) indicated the presence of host blood in explanted tissues. Immunostaining using a monoclonal antibody against Ter-119 confirmed the erythroid identity of cells in microvessels adjacent to hepatic microaggregates in explanted tissues (**Figure 6.3 C**, right). This work provides an approach to address long-standing design limitations in tissue engineering that have hindered progress of preclinical studies.

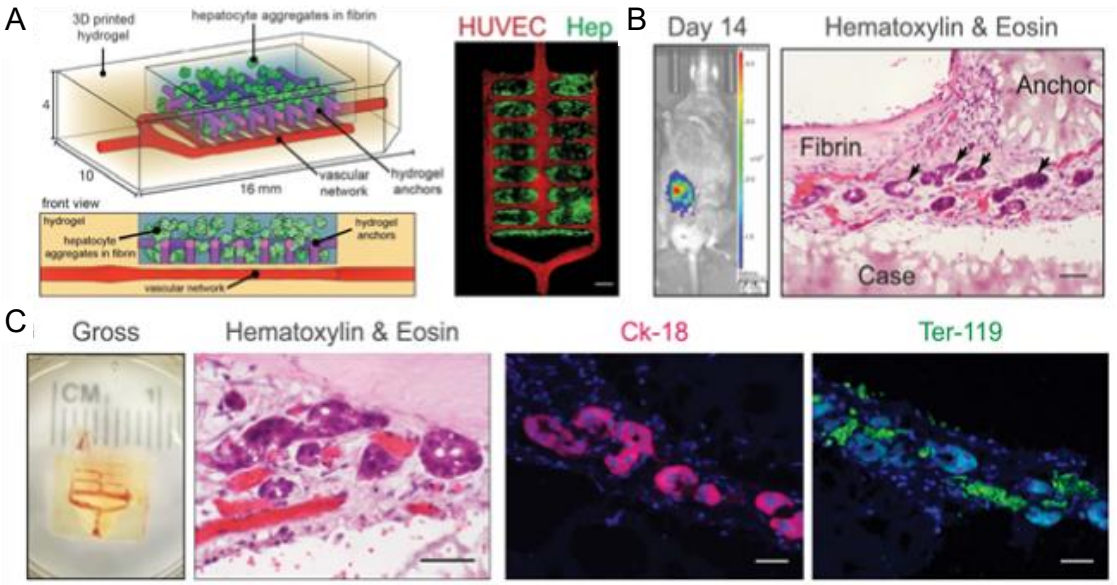

Figure 6.3. Vascularization of implanted hepatic hydrogel carriers. (**A**) (Left) Prevascularized hepatic hydrogel carriers are created by seeding endothelial cells (HUVECs) in the vascular network after printing. (Right) Confocal microscopy observations show that hydrogel anchors hysically entrap fibrin gel containing the hepatocyte aggregates (Hep) (scale bar, 1 mm). (**B**) Hepatocytes in prevascularized hepatic hydrogel carriers exhibit albumin promoter activity after implantation in mice with chronic liver injury. Graft sections stained with H&E show positioning of hepatic aggregates (black arrows) relative to printed (case, anchor) and nonprinted (fibrin) components of the carrier system (scale bar, 50 mm). (**C**) Hydrogel carriers are infiltrated with host blood (gross, H&E). Carriers contain aggregates that express the marker cytokeratin-18 (Ck-18) and are in close proximity to Ter-119–positive RBCs (scale bars, 40 mm)

6.3.2 *In Vivo implantation of HEAT-modulated artificial tissues*

To test whether gene patterning could be maintained after engraftment of artificial tissues in vivo, we stimulated tissues with HEAT and implanted these tissues into athymic mice. All tissues contained HEK293T cells expressing fLuc under the control of the heat-inducible HSPA6

promoter. All tissue constructs contained a single channel, and were stimulated in one of three ways: 1) thermofluidic perfusion at 44ºC for 60 min, 2) bulk heating in a cell culture incubator at 44ºC for 60 min, or 3) bulk exposure in a cell culture incubator to 37ºC. Tissues were implanted into mice immediately after heating and bioluminescence imaging was performed 24 hours later . We found that thermofluidic spatial control of gene expression was maintained after in vivo tissue engraftment (**Figure 6.4**).

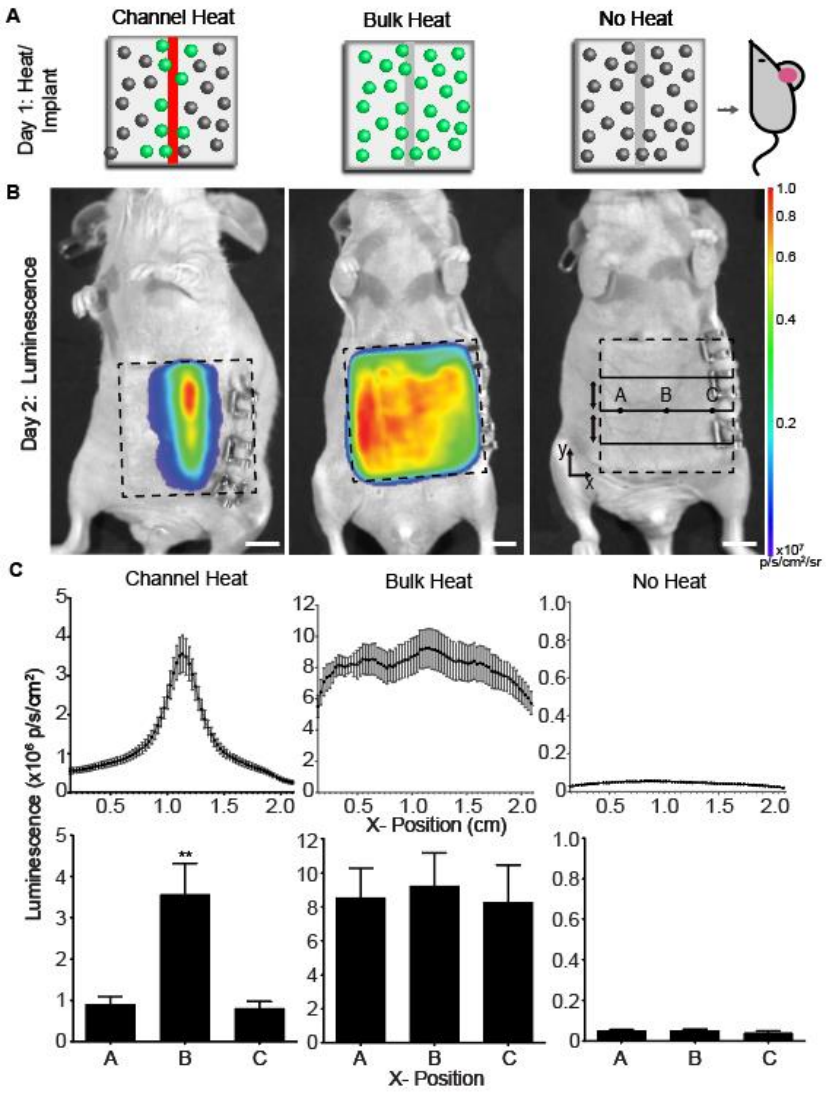

Figure 6.4. HEAT gene patterning is maintained after tissue implant in vivo. (**A**) Artificial tissues with embedded heat-inducible fLuc HEK293T cells received 44°C thermofluidic heating (channel heat, n = 5), 44°C global heating (bulk heat, n = 3), or remained at 37°C (no heat, n = 3) for 1 hour before immediate implantation into athymic mice. (**B**) Bioluminescence from implanted hydrogels (dashed lines) showed region specific signal only in channel heated hydrogels. (**C**) Average line profiles (top) across the width (x) of the hydrogel for inlet, middle, and outlet positions show that only channel heated gels induced a spatially coordinated response that

was statistically significant (bottom) between the center (position B) and edges of the hydrogel (position A and C; channel heat, n = 5; bulk heat, n = 3; no heat, n = 3; data are mean luminescence ± standard error; **P < 0.01, by one-way ANOVA

6.3.3 *Spatial control of Wnt/β-catenin signaling pathway*

As a final step, we sought to demonstrate the modularity of our system for spatially regulating expression of the Wnt/β-catenin signaling pathway, which directs diverse aspects of embryonic development, tissue homeostasis, regeneration, and disease[129]. We engineered heat-inducible constructs to drive expression of three genes in the Wnt/β-catenin signaling pathway: 1) R-spondin-1 (RSPO1), a potent positive regulator of Wnt/β-catenin signaling[130], 2) β-catenin, a critical transcriptional co-regulator that translates to the nucleus upon canonical Wnt signaling[131], and 3) Wnt-2, a ligand that binds to membrane-bound receptors to activate the Wnt/β-catenin signaling pathway[132]. The Wnt-2 gene was also tagged with the V5 protein tag. We engineered lentiviral constructs in which RSPO1, β-catenin, or Wnt2-V5 is driven by the heat-inducible HSPA6 promoter and mCherry is driven by a constitutive promoter (spleen focus-forming virus, SFFV; **Figure 6.5 A**). RT-qPCR analysis of each engineered cell line for mCherry expression relative to GAPDH expression suggested lentiviral integration (**Figure 6.5 B**).

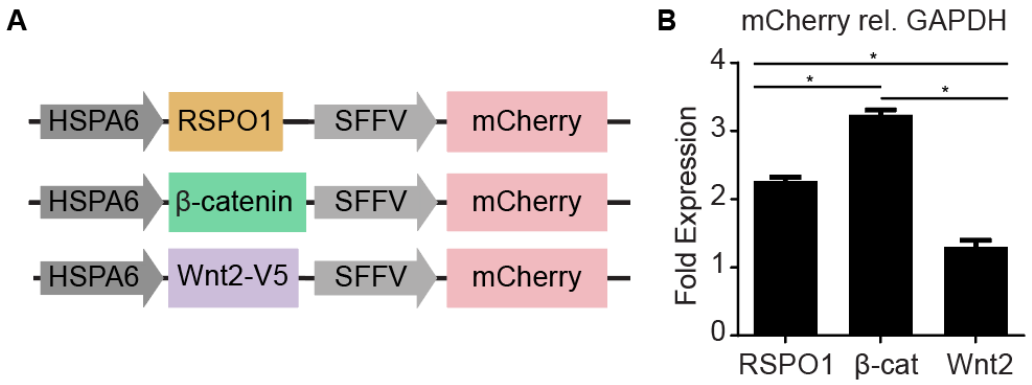

Figure 6.5. Lentiviral engineering of HEK293T cells with HEAT-inducible Wnt. (**A**) Schematics of heat shock promoter inducible Wnt lentiviral constructs. (**B**) Variations in mCherry expression are observed between individual heat-inducible HEK293T cells indicating different levels of promoter integration (n = 3, data are mean fold ± standard error, *p<0.05 by one-way ANOVA followed by Tukey's multiple comparison test).

We then printed artificial tissues containing heat-inducible β-catenin, RSPO1, or Wnt2 HEK293T cells and a single fluidic channel. Constructs were heated fluidically and then sliced into longitudinal zones (**Figure 6.6 A**) to analyze expression of the Wnt family gene expression by RT-qPCR. Representative artificial tissues contained mCherry positive cells across the tissue (**Figure 6.6 B**). Immunostaining for the V5 tag fused to Wnt2 appeared higher near the heated channel compared to the gel periphery (Fig 6C). R-spondin-1, β-catenin, or Wnt2 expression was highest in the zone surrounding the heated channel (**Figure 6.6 C**). These results show that HEAT can be leveraged to activate expression of various family members of the Wnt/β-catenin signaling pathway.

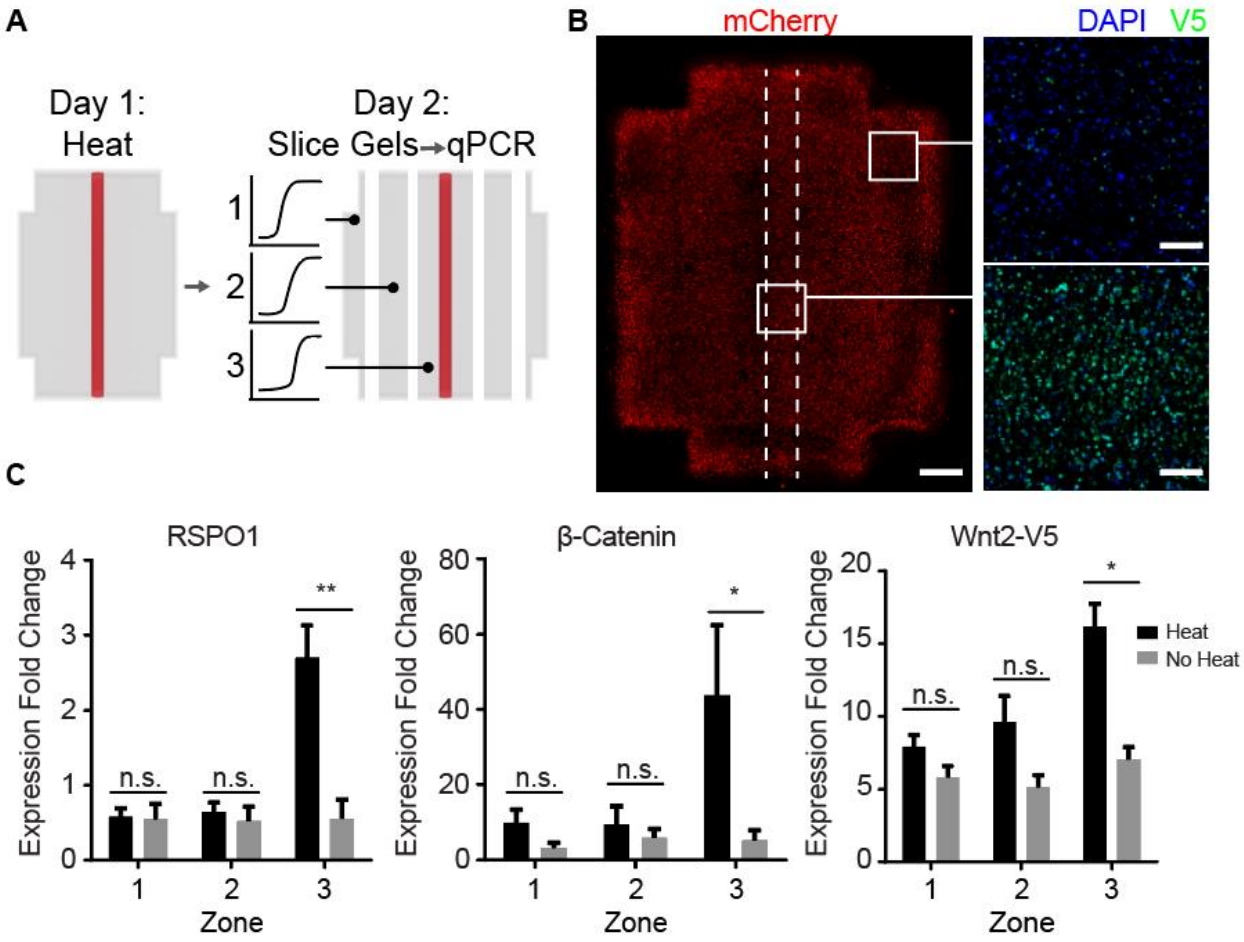

Figure 6.6. Thermofluidic Wnt regulation in engineered HEK293T cells. (**A**) Schematic of thermofluidic RT-qPCR experiments. (**B**) mCherry+ HEK293T cells in printed tissues (left). Scale bars, 1 mm. Images of thermofluidically heated Wnt2 constructs after immunostaining for V5 tag (coexpressed with Wnt2; right; images taken near the tissue's channel and periphery as indicated by insets). Scale bars, 200 µm. (**C**) Wnt family genes were up-regulated in zone 3 of thermofluidically perfused gels compared to controls (n = 4, mean fold change ± standard error; *P < 0.05 and **P < 0.01 by two-way ANOVA followed by Tukey's multiple comparison test).

6.3.4 *Effect of thermofluidic activation of RSPO1 on the expression of key metabolic liver enzymes*

We reasoned that the ability to activate expression of Wnt/β-catenin signaling pathway members could be useful for the emerging human "organ-on-a-chip" field, by affecting functional cellular phenotypes in vitro. To test this, we turned to the liver, which performs hundreds of metabolic functions essential for life, including central roles in drug metabolism. To carry out these functions, hepatocytes divide the labor, with hepatocytes in different spatial locations performing different functions, a phenomenon called liver zonation. Recent studies have shown that liver zonation is regulated at the molecular level by Wnt/β-catenin signaling[131], with higher Wnt activity associated with a pericentral vein phenotype and lower Wnt activity characteristic of a periportal phenotype. However, the extent to which different members of this pathway affect human zonated hepatic phenotypes remains unclear. A better understanding of this process would accelerate development of zonated human liver models for hepatotoxicity and drug metabolism studies.

We hypothesized that thermofluidic activation of R-spondin-1 in human hepatic cells would be sufficient to activate zonated hepatic gene expression profiles, as ectopic expression of RSPO1 in mouse liver has recently been shown to induce a pericentral zonation phenotype in vivo[133]. To test this hypothesis, we transduced human HepaRG cells, an immortalized human hepatic cell line that retains characteristics of primary human hepatocytes, with our lentiviral construct in which HSPA6 drives RSPO1 and SFFV drives mCherry (**Figure 6.7 A**). Transduced human hepatic cells were then printed in artificial tissues with a single fluidic channel, to mimic central lobular placement of the central vein (**Figure 6.7 A**). Constructs were heated fluidically and then sliced into zones and gene expression was measured by RT-qPCR (**Figure 6.7 B**). Fold

upregulation values were normalized to identically fabricated control artificial tissues maintained at 37 °C. We found that RSPO1 expression increased in a dose-dependent and spatially defined manner, with expression in Zone 3 nearest the channel ("central vein") 10-fold higher than in Zone 1 by one-hour post heating. RSPO1 expression was transient, falling with each day after heating, like our luciferase studies (**Figure 6.7 B**).

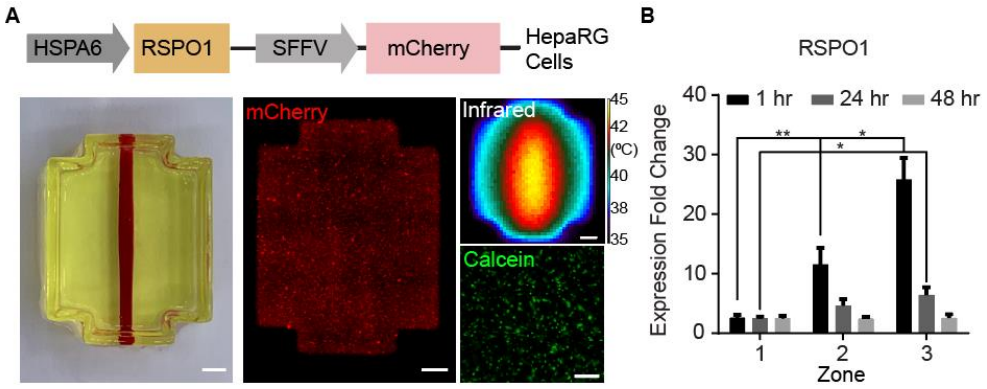

Figure 6.7. Thermofluidic RSPO1 regulation in engineered HepaRG cells. (**A**) Differentiated HepaRG cells were engineered with a heat-inducible RSPO1 construct (schematic, top) and printed in single-channel hydrogels (photograph, left). Scale bars, 1 mm. After heating (infrared), HepaRGs remained viable in printed constructs (calcein). Scale bar, 200 □m. (**B**) Thermofluidically heated RSPO-1 HepaRG hydrogels were dissected into zones 1 to 3 based on distance from the heat channel for RT-qPCR analysis at 1, 24, and 48 hours after heating. Expression fold change was normalized to no heat control samples. qPCR analysis of RSPO-1 across dissected zones (n = 5 to 10, data are mean fold change ± standard error; *P < 0.05 by one-way ANOVA followed by Tukey's multiple comparison test).

Importantly, thermofluidic activation of RSPO1 induced expression of key pericentral marker genes, including glutamine synthetase, an enzyme involved in nitrogen metabolism, and

the cytochrome P450 (CYP) drug-metabolizing enzymes CYP1A2, CYP1A1, and CYP2E1 relative to control tissues that were not heated, though with varied timing and without spatial localization in this study (**Figure 6.8 A**).

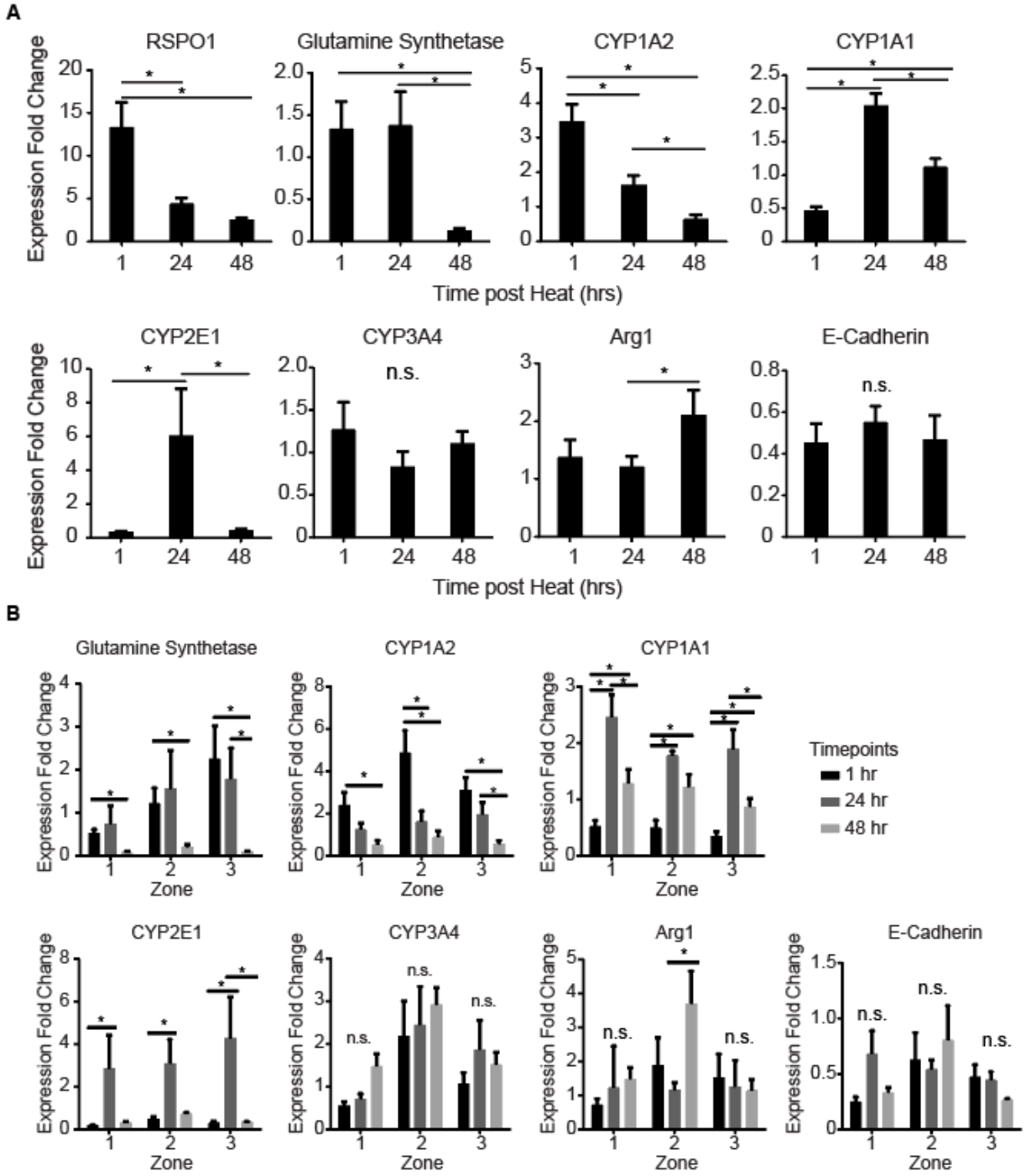

Figure 6.8. Thermofluidic RSPO1 induction modulates phase I drug metabolism expression. (**A**) RT-qPCR analysis of pooled RNA across all zones at each time point for pericentral associated genes, glutamine synthetase, CYP1A2, CYP1A1, CYP2E1, and CYP3A4, and periportal/midzonal genes, Arg1 and E-cadherin (n = 15 to 30, data are

mean fold change ± standard error, **P < 0.01 and *P < 0.05 by one-way ANOVA followed by Tukey's multiple comparison test). n.s., not significant. **B**, Zonal expression profiles for pericentral (Glutamine Synthetase, CYP1A2, CYP1A1, CYP2E1, CYP3A4) and periportal/midzonal (E-Cadherin, Arg1) genes assayed in heat-induced RSPO1 HepaRG at different times post heating. Temporal upregulation of canonical pericentral Wnt responsive genes (Glutamine Synthetase, CYP1A2) is seen at 1 and 24 hours and CYP2E1 at 24 hours in comparison to 48 hours after for Zones 1, 2, and 3. Trending spatial zonation patterns (increase in expression from Zone 1 to Zone 3) are seen for Glutamine Synthetase and CYP2E1, but these were not statistically significant. Periportal/midzonal gene Arg1 shows significant upregulation in Zone 2 for the 48 hour timepoint in comparison to the 1 hour and 24 hour timepoint, while periportal E-cadherin shows no zonal differences (n = 15 - 30, data are mean fold change ± standard error, *p<0.05 by two-way ANOVA followed by Tukey's multiple comparison test).

Expression of pericentral drug-metabolizing enzyme CYP3A4 was not induced with heating, consistent with other studies in which adding Wnt3a ligand to primary human hepatocyte cultures did not alter CYP3A4 expression[134]. Periportal marker E-Cadherin was not induced, but periportal/midzonal gene Arg-1 increased at 48 hours, especially in the Zone 2 midzonal region (**Figure 6.8 B**). Taken together, these studies contribute a fundamental understanding of how various liver zonation genes are induced by RSPO1 activation in human hepatic cells.

6.4 Discussion & Conclusions

To fully realize the vision of precision-controlled 3D artificial tissues, a diverse toolkit of orthogonal physical delivery and molecular remote control agents will likely be needed[32,91].

Thermofluidics could be coupled with other tissue engineering strategies that program extracellular[103–105] or intracellular[96,135] signal presentation, cell patterning[111], or tissue curvature[136]. Thermofluidics could also be used orthogonally with other remote-control agents, such as those leveraging small molecule[98], ultrasound[41], radio wave[48], magnetic[137], or light-based activation[138]. Coupled with rapid advances in gene editing[95], synthetic morphogenesis[90,139], and stem cell technology[92,140], thermofluidics could be useful for spatially and temporally activating genes across tissues to drive cell proliferation, fate or assembly decisions. While we demonstrate utility for activating Wnt/β-catenin signaling pathway genes here, this approach could be rapidly adapted to activate any gene of interest. In our studies, we demonstrate one application of this approach, by driving human hepatic cells towards a more pericentral liver phenotype in 3D artificial tissues. In doing so, we gain fundamental insights into how activation of Wnt agonist RSPO1 regulates expression of various metabolic zonation genes. These findings have important implications for developing both organ-on-chip systems for pharmacology and hepatotoxicity, as well as artificial tissues for human therapy. By blurring the interface between the advanced fabrication and biological realms, thermofluidics thus creates a new avenue for bioactive tissues with applications in both basic and translational biomedicine.

Chapter 7. CONCLUSIONS AND FUTURE DIRECTIONS

To address problems in human health, research and industry are developing new biotechnologies at an accelerating rate. Tissue engineering, a branch of regenerative medicine is leveraging this rapid development to enhance control and readout capabilities of artificial tissue systems. This thesis is a case study of an ongoing transformation in tissue engineering. In this work we present two novel technological platforms that are designed for tissue engineering, but derive from key innovations in additive manufacturing (3D printing) and molecular biology (gene editing). In Chapter 3, we detail our SLATE platform (stereolithographic apparatus for tissue engineering) as a biofabrication method for generating complex, mesoscale vasculature in 3D printed hydrogel tissues. We find that the inclusion of biocompatible photo absorbing agents, derived from natural and synthetic food dyes, is critical to SLATE's ability to fabricate patent vascular channels. We implement SLATE to fabricate architecturally defined 'hydrogel carriers' of hepatic tissue that survive and engraft in mouse models of liver injury. In Chapter 4, we present a paired platform; "Thermofluidics" that employs fluid-based heat transfer to coordinate thermal gradients spatially and temporally in 3D engineered tissues. From computational and physical modelling, we find that the geometry of temperature fields in thermofluidically treated tissues is predictable from key features such as tissue size and channel geometry; as well as other important factors such as fluid temperature, fluid flow rate and environmental temperature.

In Chapter 5, we combine Thermofluidics with engineered heat-inducible cells to deliver our HEAT platform (heat exchangers for actuation of transcription). We genetically modified human cells for transgene expression in response to defined hyperthermic windows which we characterized empirically. By encapsulating heat-inducible cells in perfusable 3D tissues and we create three dimensional zones of gene expression. We demonstrate that these zones follow a

gradient like pattern that can be modulated by changing heat delivery schemas. Finally, in Chapter 6 we apply our platforms to the challenge of creating zonated liver tissue. Adapting our genetic engineering system for production of members of the Wnt family of proteins, we demonstrate that artificial production of Wnt family proteins in hepatic cell lines can recapitulate aspects of a zonated gene expression profile.

In summation, the platforms presented and described in this work are unique contributions to the growing sphere of biotechnologies. The ability to operate within biological phenomena at the appropriate physical and temporal scales is ever-increasing. Knowledge we gain from studying biology naturally gives rise to an impetus to replicate the phenomena in engineered systems. Through these engineering efforts we manifest new phenomena that redefines what we consider as "natural" or even "possible". In turn, our co current advances in our knowledge and technology create a beautiful self-sustaining cycle that has limitless potential for good.

Future applications should seek to deepen and broaden the capabilities of the systems presented here. For example, computational thermal modeling can be extended by methodically altering parameters used in heat exchanger design to a broad library of parameterized 'thermal shapes', which researchers can later mine to construct desired gene expression gradients. Further advancements in molding thermal gradients can be achieved through materials engineering. By modulating the thermal properties and interfaces between hydrogel tissue components, different temperature ranges and profiles can be generated. One technique to achieve this could be to tether heat-dissipating nanoparticles within the hydrogel backbone that can act as local transducers for heat to provide for higher spatial resolution. Finally, we anticipate that substantial technology progress will be made on the molecular editing end. The ability to design and predict

DNA level interactions and expression kinetics in shorter and shorter time windows is accelerating progress into new stimuli-response genetic control elements that operate at multiple levels in the protein production process. We hope that this work provides a springboard for future researchers and scientists to develop new innovations that heal, inform, and inspire.

REFERENCES

1. Moroni, L. *et al.* Biofabrication strategies for 3D in vitro models and regenerative medicine. *Nat. Rev. Mater.* **3**, 21–37 (2018).
2. Rosso, F., Giordano, A., Barbarisi, M. & Barbarisi, A. From Cell-ECM interactions to tissue engineering. *J. Cell. Physiol.* **199**, 174–180 (2004).
3. Armstrong, J. P. K. & Stevens, M. M. Emerging Technologies for Tissue Engineering: From Gene Editing to Personalized Medicine. *Tissue Eng. - Part A* **25**, 688–692 (2019).
4. Ungrin, M. D., Joshi, C., Nica, A., Bauwens, C. & Zandstra, P. W. Reproducible, Ultra High-Throughput Formation of Multicellular Organization from Single Cell Suspension-Derived Human Embryonic Stem Cell Aggregates. *PLoS One* **3**, e1565 (2008).
5. Pham, Q. P., Sharma, U. & Mikos, A. G. Electrospinning of Polymeric Nanofibers for Tissue Engineering Applications: A Review. *Tissue Eng.* **12**, 1197–1211 (2006).
6. Kodama, H. Automatic method for fabricating a three-dimensional plastic model with photo-hardening polymer. *Rev. Sci. Instrum.* **52**, 1770–1773 (1981).
7. Murphy, S. V. & Atala, A. 3D bioprinting of tissues and organs. *Nat. Biotechnol.* **32**, 773–785 (2014).
8. Atala, A. & Forgacs, G. Three-Dimensional Bioprinting in Regenerative Medicine: Reality, Hype, and Future. *Stem Cells Transl. Med.* **8**, 744–745 (2019).
9. Miller, J. S. The Billion Cell Construct: Will Three-Dimensional Printing Get Us There? *PLoS Biol.* **12**, e1001882 (2014).
10. Dasgupta, Q. & Black, L. D. A FRESH SLATE for 3D bioprinting. *Science (80-.).* **365**, 446–447 (2019).
11. Grigoryan, B. *et al.* Multivascular networks and functional intravascular topologies within biocompatible hydrogels. *Science (80-.).* **364**, 458–464 (2019).
12. Lee, A. *et al.* 3D bioprinting of collagen to rebuild components of the human heart. *Science (80-.).* **365**, 482–487 (2019).
13. Kelly, B. E. *et al.* Volumetric additive manufacturing via tomographic reconstruction. *Science (80-.).* **363**, 1075–1079 (2019).
14. Hinton, T. J. *et al.* Three-dimensional printing of complex biological structures by freeform reversible embedding of suspended hydrogels. *Sci. Adv.* **1**, e1500758 (2015).

15. Dasgupta, Q. & Black, L. D. A FRESH SLATE for 3D bioprinting. *Science (80-.).* **365**, 446–447 (2019).
16. Skylar-Scott, M. A. *et al.* Biomanufacturing of organ-specific tissues with high cellular density and embedded vascular channels. *Sci. Adv.* **5**, (2019).
17. Arakawa, C. K., Badeau, B. A., Zheng, Y. & DeForest, C. A. Multicellular Vascularized Engineered Tissues through User-Programmable Biomaterial Photodegradation. *Adv. Mater.* **29**, 1703156 (2017).
18. Kinstlinger, I. S. *et al.* Generation of model tissues with dendritic vascular networks via sacrificial laser-sintered carbohydrate templates. *Nat. Biomed. Eng.* **4**, 916–932 (2020).
19. Dudley, D., Duncan, W. M. & Slaughter, J. Emerging digital micromirror device (DMD) applications. in *MOEMS Display and Imaging Systems* (ed. Urey, H.) **4985**, 14 (2003).
20. Tumbleston, J. R. *et al.* Continuous liquid interface production of 3D objects. *Science (80-.).* **347**, 1349–1352 (2015).
21. Lin, H. *et al.* Application of visible light-based projection stereolithography for live cell-scaffold fabrication with designed architecture. *Biomaterials* **34**, 331–339 (2013).
22. Ma, X. *et al.* Deterministically patterned biomimetic human iPSC-derived hepatic model via rapid 3D bioprinting. *Proc. Natl. Acad. Sci.* **113**, 2206–2211 (2016).
23. Nichol, J. W. *et al.* Biomaterials Cell-laden microengineered gelatin methacrylate hydrogels. *Biomaterials* **31**, 5536–5544 (2010).
24. Sun, C., Fang, N., Wu, D. M. & Zhang, X. Projection micro-stereolithography using digital micro-mirror dynamic mask. *Sensors Actuators, A Phys.* **121**, 113–120 (2005).
25. Ligon, S. C., Liska, R., Stampfl, J., Gurr, M. & Mülhaupt, R. Polymers for 3D Printing and Customized Additive Manufacturing. *Chem. Rev.* **117**, 10212–10290 (2017).
26. Truby, R. L. & Lewis, J. A. Printing soft matter in three dimensions. *Nature* **540**, 371–378 (2016).
27. Bernal, P. N. *et al.* Volumetric Bioprinting of Complex Living-Tissue Constructs within Seconds. *Adv. Mater.* **31**, 1904209 (2019).
28. Loterie, D., Delrot, P. & Moser, C. High-resolution tomographic volumetric additive manufacturing. *Nat. Commun.* **11**, 1–6 (2020).
29. Hoffman, T. *et al.* Synthetic Biology and Tissue Engineering: Toward Fabrication of Complex and Smart Cellular Constructs. *Adv. Funct. Mater.* **1909882**, 1–20 (2020).

30. Gossen, M. & Bujardt, H. Tight control of gene expression in mammalian cells by tetracycline-responsive promoters. **89**, 5547–5551 (1992).
31. Boyden, E. S., Zhang, F., Bamberg, E., Nagel, G. & Deisseroth, K. Millisecond-timescale, genetically targeted optical control of neural activity. *Nat. Neurosci.* **8**, 1263–1268 (2005).
32. Toettcher, J. E., Voigt, C. A., Weiner, O. D. & Lim, W. A. The promise of optogenetics in cell biology: interrogating molecular circuits in space and time. *Nat. Methods* **8**, 35–38 (2011).
33. Pastrana, E. Optogenetics: Controlling cell function with light. *Nat. Methods* **8**, 24–25 (2011).
34. Ye, H., Baba, M. D.-E., Peng, R.-W. & Fussenegger, M. A Synthetic Optogenetic Transcription Device Enhances Blood-Glucose Homeostasis in Mice. *Science*- **332**, 1565–1568 (2011).
35. Ash, C., Dubec, M., Donne, K. & Bashford, T. Effect of wavelength and beam width on penetration in light-tissue interaction using computational methods. *Lasers Med. Sci.* **32**, 1909–1918 (2017).
36. Park, S. Il *et al.* Stretchable multichannel antennas in soft wireless optoelectronic implants for optogenetics. *Proc. Natl. Acad. Sci.* **113**, E8169–E8177 (2016).
37. Jeong, J. W. *et al.* Wireless Optofluidic Systems for Programmable In Vivo Pharmacology and Optogenetics. *Cell* **162**, 662–674 (2015).
38. Shao, J. *et al.* Smartphone-controlled optogenetically engineered cells enable semiautomatic glucose homeostasis in diabetic mice. *Sci. Transl. Med.* **9**, eaal2298 (2017).
39. Shao, J. *et al.* Synthetic far-red light-mediated CRISPR-dCas9 device for inducing functional neuronal differentiation. *Proc. Natl. Acad. Sci. U. S. A.* **115**, E6722–E6730 (2018).
40. Zhu, L., Wu, Y., Yoon, C. W. & Wang, Y. Mechanogenetics for cellular engineering and cancer immunotherapy. *Curr. Opin. Biotechnol.* **66**, 88–94 (2020).
41. Pan, Y. *et al.* Mechanogenetics for the remote and noninvasive control of cancer immunotherapy. *Proc. Natl. Acad. Sci.* **115**, 992–997 (2018).
42. Alsberg, E., Feinstein, E., Joy, M. P., Prentiss, M. & Ingber, D. E. Magnetically-Guided Self-Assembly of Fibrin Matrices with Ordered Nano-Scale Structure for Tissue Engineering. *Tissue Eng.* **12**, 3247–3256 (2006).

43. Tasoglu, S. *et al.* Magnetic Levitational Assembly for Living Material Fabrication. *Adv. Healthc. Mater.* **4**, 1469–1476 (2015).
44. Bielawski, K. S., Leonard, A., Bhandari, S., Murry, C. E. & Sniadecki, N. J. Real-Time Force and Frequency Analysis of Engineered Human Heart Tissue Derived from Induced Pluripotent Stem Cells Using Magnetic Sensing. *Tissue Eng. - Part C Methods* **22**, 932–940 (2016).
45. Dobson, J. Remote control of cellular behaviour with magnetic nanoparticles. *Nat. Nanotechnol.* **3**, 139–143 (2008).
46. Etoc, F. *et al.* Magnetogenetic control of protein gradients inside living cells with high spatial and temporal resolution. *Nano Lett.* **15**, 3487–3494 (2015).
47. Lißе, D. *et al.* Engineered Ferritin for Magnetogenetic Manipulation of Proteins and Organelles Inside Living Cells. *Adv. Mater.* **29**, (2017).
48. Stanley, S. A., Sauer, J., Kane, R. S., Dordick, J. S. & Friedman, J. M. Remote regulation of glucose homeostasis in mice using genetically encoded nanoparticles. **21**, (2015).
49. Pan, Y., Yoon, S., Zhu, L. & Wang, Y. Acoustic mechanogenetics. *Curr. Opin. Biomed. Eng.* **7**, 64–70 (2018).
50. Rossi, F. M. V. & Blau, H. M. Recent advances in inducible gene expression systems. *Curr. Opin. Biotechnol.* **9**, 451–456 (1998).
51. Elowitz, M. & Lim, W. A. Pme_2010. 9–10 doi:10.1038/468889a
52. Lindquist, S. The Heat-Shock Response. *Annu. Rev. Biochem.* **55**, 1151–1191 (1986).
53. Åkerfelt, M., Morimoto, R. I. & Sistonen, L. Heat shock factors: integrators of cell stress, development and lifespan. **11**, 545–555 (2010).
54. Feng, J., Wang, X., Liao, Y., Feng, J. & Tang, L. A novel conditional gene silencing method using a tumor - specific and heat - inducible siRNA system. *J. Ind. Microbiol. Biotechnol.* **43**, 761–770 (2016).
55. Martín-Saavedra, F. M., Voellmy, R., Vilaboa, N., Franceschi, R. T. & Wilson, C. G. Spatiotemporal Control of Vascular Endothelial Growth Factor Expression Using a Heat-Shock-Activated, Rapamycin-Dependent Gene Switch. *Hum. Gene Ther. Methods* **24**, 160–170 (2013).
56. Kamei, Y. *et al.* Infrared laser – mediated gene induction in targeted single cells in vivo. **6**, 3–4 (2009).

57. Moncion, A. *et al.* Spatiotemporally-controlled transgene expression in hydroxyapatite-fibrin composite scaffolds using high intensity focused ultrasound. *Biomaterials* **194**, 14–24 (2019).
58. Wang, X., Chen, X. & Yang, Y. Spatiotemporal control of gene expression by a light-switchable transgene system. **9**, (2012).
59. Miyako, E. *et al.* Photothermic regulation of gene expression triggered by laser-induced carbon nanohorns. **109**, (2012).
60. Deckers, R. *et al.* Image-guided, noninvasive, spatiotemporal control of gene expression. (2008).
61. Smith, R. C., Machluf, M., Bromley, P., Atala, A. & Walsh, K. Spatial and Temporal Control of Transgene Expression Through Ultrasound-Mediated Induction of the Heat Shock Protein 70B Promoter In Vivo. *Hum. Gene Ther.* **13**, 697–706 (2002).
62. Wilson, C. G. *et al.* Patterning Expression of Regenerative Growth Factors Using High Intensity Focused Ultrasound. **20**, 769–779 (2014).
63. Yin, P. T. *et al.* Biomaterials Stem cell-based gene therapy activated using magnetic hyperthermia to enhance the treatment of cancer. *Biomaterials* **81**, 46–57 (2016).
64. Yamaguchi, M., Ito, A., Ono, A., Kawabe, Y. & Kamihira, M. Heat-Inducible Gene Expression System by Applying Alternating Magnetic Field to Magnetic Nanoparticles. (2014).
65. Lee-Gosselin, A., Abedi, M. H., Moser, B. A., Shapiro, M. G. & Piraner, D. I. Tunable thermal bioswitches for in vivo control of microbial therapeutics. *Nat. Chem. Biol.* **13**, 75–80 (2016).
66. Kaczmarek, K. *et al.* Heating Induced by Therapeutic Ultrasound in the Presence of Magnetic Nanoparticles. (2018). doi:10.1021/acsami.8b02496
67. Piraner, D. I., Abedi, M. H., Moser, B. A., Lee-gosselin, A. & Shapiro, M. G. Tunable thermal bioswitches for in vivo control of microbial therapeutics. *Nat. Publ. Gr.* **13**, (2016).
68. Abedi, M. H., Lee, J., Piraner, D. I. & Shapiro, M. G. Thermal Control of Engineered T-cells. *ACS Synth. Biol.* **9**, 1941–1950 (2020).
69. Monahan-earley, R. *et al. Evolutionary origins of the blood vascular system and endothelium*. **11**, (2017).

70. Scott, G. R. Elevated performance: the unique physiology of birds that fly at high altitudes. *J. Exp. Biol.* **214**, 2455–2462 (2011).
71. Farmer, C. G. The Evolution of Unidirectional Pulmonary Airflow. *Physiology* **30**, 260–272 (2015).
72. Tumbleston, J. R. *et al.* Continuous liquid interface production of 3D objects. **347**, 635–639 (2015).
73. Kelly, B. E., Bhattacharya, I., Heidari, H. & Shusteff, M. Volumetric additive manufacturing via tomographic reconstruction. **d**, 1075–1079 (2019).
74. Miller, J. S. *et al.* Rapid casting of patterned vascular networks for perfusable engineered three-dimensional tissues. *Nat. Mater.* **11**, 768–774 (2012).
75. Bhattacharjee, T. *et al.* Writing in the granular gel medium. *Sci. Adv.* **1**, e1500655 (2015).
76. Kolesky, D. B. *et al.* 3D Bioprinting of Vascularized, Heterogeneous Cell-Laden Tissue Constructs. *Adv. Mater.* **26**, 3124–3130 (2014).
77. Kang, H. *et al.* A 3D bioprinting system to produce human-scale tissue constructs with structural integrity. *Nat. Biotechnol.* **34**, (2016).
78. Tsang, V. L. *et al.* Fabrication of 3D hepatic tissues by additive photopatterning of cellular hydrogels. *FASEB J.* **21**, 790–801 (2007).
79. Neiman, J. A. S. *et al.* Photopatterning of hydrogel scaffolds coupled to filter materials using stereolithography for perfused 3D culture of hepatocytes. *Biotechnol. Bioeng.* **112**, 777–787 (2015).
80. Hahn, M. S., Miller, J. S. & West, J. L. Three-Dimensional Biochemical and Biomechanical Patterning of Hydrogels for Guiding Cell Behavior. *Adv. Mater.* **18**, 2679–2684 (2006).
81. DeForest, C. A. & Anseth, K. S. Cytocompatible click-based hydrogels with dynamically tunable properties through orthogonal photoconjugation and photocleavage reactions. *Nat. Chem.* **3**, 925–931 (2011).
82. Heintz, K. A. *et al.* Fabrication of 3D Biomimetic Microfluidic Networks in Hydrogels. *Adv. Healthc. Mater.* **5**, 2153–2160 (2016).
83. Fonovich, T. M. Sudan dyes: are they dangerous for human health? *Drug Chem. Toxicol.* **36**, 343–352 (2013).
84. Miller, J. S. *et al.* Biomaterials Bioactive hydrogels made from step-growth derived PEG

– peptide macromers. *Biomaterials* **31**, 3736–3743 (2010).

85. Fairbanks, B. D., Schwartz, M. P., Bowman, C. N. & Anseth, K. S. Photoinitiated polymerization of PEG-diacrylate with lithium phenyl-2,4,6-trimethylbenzoylphosphinate: polymerization rate and cytocompatibility. *Biomaterials* **30**, 6702–6707 (2009).
86. Shirahama, H., Lee, B. H., Tan, L. P. & Cho, N. Precise Tuning of Facile One-Pot Gelatin Methacryloyl (GelMA) Synthesis. *Nat. Publ. Gr.* 1–11 (2016). doi:10.1038/srep31036
87. Stevens, L. J., Burgess, J. R., Stochelski, M. A. & Kuczek, T. Amounts of Artificial Food Dyes and Added Sugars in Foods and Sweets Commonly Consumed by Children. (2015). doi:10.1177/0009922814530803
88. Beik, J., Abed, Z., Shakeri-Zadeh, A., Nourbakhsh, M. & Shiran, M. B. Evaluation of the sonosensitizing properties of nano-graphene oxide in comparison with iron oxide and gold nanoparticles. *Phys. E Low-Dimensional Syst. Nanostructures* **81**, 308–314 (2016).
89. Green, J. J. & Elisseeff, J. H. Mimicking biological functionality with polymers for biomedical applications. *Nature* **540**, 386–394 (2016).
90. Vogt, N. Customizing cell-cell communication. *Nat. Methods* **13**, 285–285 (2016).
91. Morsut, L. *et al.* Engineering Customized Cell Sensing and Response Behaviors Using Synthetic Notch Receptors. *Cell* **118**, 6072–6078 (2016).
92. Warmflash, A., Sorre, B., Etoc, F., Siggia, E. D. & Brivanlou, A. H. A method to recapitulate early embryonic spatial patterning in human embryonic stem cells. *Nat. Methods* **11**, 847–854 (2014).
93. Chang, N. *et al.* Genome editing with RNA-guided Cas9 nuclease in Zebrafish embryos. *Cell Res.* **23**, 465–472 (2013).
94. Cong, L. *et al.* Multiplex Genome Engineering Using CRISPR/Cas Systems. *Science (80-.).* **339**, 819–823 (2013).
95. Barrangou, R. & Doudna, J. A. Applications of CRISPR technologies in research and beyond. *Nat. Biotechnol.* **34**, 933–941 (2016).
96. Polstein, L. R. & Gersbach, C. A. A light-inducible CRISPR-Cas9 system for control of endogenous gene activation. **11**, (2015).
97. Ntziachristos, V. Going deeper than microscopy : the optical imaging frontier in biology. *Nat. Methods* **7**, 603–614 (2010).
98. Deans, T. L., Singh, A., Gibson, M. & Elisseeff, J. H. Regulating synthetic gene networks

in 3D materials. *Proc. Natl. Acad. Sci.* **109**, 15217–15222 (2012).

99. Lipkin, M. & Hardy, D. Measurement of Some Thermal Properties of Human Tissues. *J. Appl. Physiol.* **7**, 212–217 (1954).
100. Gamboa, L. *et al.* Heat-Triggered Remote Control of CRISPR-dCas9 for Tunable Transcriptional Modulation. (2020). doi:10.1021/acschembio.9b01005
101. Dreano, M. *et al.* High-level, heat-regulated synthesis of proteins in eukaryotic cells. *Gene* **49**, 1–8 (1986).
102. Lutolf, M. P. & Hubbell, J. A. Synthetic biomaterials as instructive extracellular microenvironments for morphogenesis in tissue engineering. *Nat. Biotechnol.* **23**, 47–55 (2005).
103. Martino, M. M. *et al.* Growth Factors Engineered for Super-Affinity to the Extracellular Matrix Enhance Tissue Healing. *Science*- **343**, 885–889 (2014).
104. DeForest, C. A. & Tirrell, D. A. A photoreversible protein-patterning approach for guiding stem cell fate in three-dimensional gels. *Nat. Mater.* **14**, 523–531 (2015).
105. Lee, T. T. *et al.* Light-triggered in vivo activation of adhesive peptides regulates cell adhesion, inflammation and vascularization of biomaterials. *Nat. Mater.* **14**, 352–360 (2015).
106. Loebel, C., Mauck, R. L. & Burdick, J. A. Local nascent protein deposition and remodelling guide mesenchymal stromal cell mechanosensing and fate in three-dimensional hydrogels. *Nat. Mater.* **18**, (2019).
107. Asrani, S. K., Devarbhavi, H., Eaton, J. & Kamath, P. S. Burden of liver diseases in the world. *J. Hepatol.* **70**, 151–171 (2019).
108. Byass, P. The global burden of liver disease: a challenge for methods and for public health. *BMC Med.* **12**, 159 (2014).
109. Based on OPTN data as of January 1, 2019.
110. Agarwal, T., Subramanian, B. & Maiti, T. K. Liver Tissue Engineering: Challenges and Opportunities. *ACS Biomater. Sci. Eng.* **5**, 4167–4182 (2019).
111. Stevens, K. R. *et al.* InVERT molding for scalable control of tissue microarchitecture. *Nat. Commun.* **4**, 1847 (2013).
112. Lee, H. & Cho, D.-W. One-step fabrication of an organ-on-a-chip with spatial heterogeneity using a 3D bioprinting technology. *Lab Chip* **16**, 2618–2625 (2016).

113. Lee, J. W. *et al.* Development of a 3D cell printed construct considering angiogenesis for liver tissue engineering. *Biofabrication* **8**, (2016).
114. Grix, T. *et al.* Bioprinting Perfusion-Enabled Liver Equivalents for Advanced Organ-on-a-Chip Applications. *Genes (Basel).* **9**, 176 (2018).
115. Richard, C., Richard, C., Neild, A., Cadarso, V. J. & Cadarso, V. J. The emerging role of microfluidics in multi-material 3D bioprinting. *Lab Chip* **20**, 2044–2056 (2020).
116. Gebhardt, R. & Matz-soja, M. Liver zonation : Novel aspects of its regulation and its impact on homeostasis. **20**, 8491–8504 (2014).
117. McCarty, W. J., Usta, O. B. & Yarmush, M. L. A Microfabricated Platform for Generating Physiologically-Relevant Hepatocyte Zonation. *Sci. Rep.* **6**, 26868 (2016).
118. Ahn, J. *et al.* Human three-dimensional in vitro model of hepatic zonation to predict zonal hepatotoxicity. *J. Biol. Eng.* **13**, 1–15 (2019).
119. Behari, J. The Wnt/β-catenin signaling pathway in liver biology and disease. *Expert Rev. Gastroenterol. Hepatol.* **4**, 745–756 (2010).
120. Wahlicht, T. *et al.* Controlled Functional Zonation of Hepatocytes In Vitro by Engineering of Wnt Signaling. *ACS Synth. Biol.* **9**, 1638–1649 (2020).
121. Seglen, P. O. Preparation of Isolated Rat Liver Cells. *Methods Cell Biol.* **13**, 29--83 (1976).
122. Stevens, K. R. *et al.* In situ expansion of engineered human liver tissue in a mouse model of chronic liver disease. *Sci. Transl. Med.* **9**, (2017).
123. Kolligs, F. T., Hu, G., Dang, C. V. & Fearon, E. R. Neoplastic Transformation of RK3E by Mutant β-Catenin Requires Deregulation of Tcf/Lef Transcription but Not Activation of c- myc Expression. *Mol. Cell. Biol.* **19**, 5696–5706 (1999).
124. MacDonald, B. T. *et al.* Disulfide Bond Requirements for Active Wnt Ligands. *J. Biol. Chem.* **289**, 18122–18136 (2014).
125. Klose, A. D. & Paragas, N. Automated quantification of bioluminescence images. *Nat. Commun.* **9**, 4262 (2018).
126. Li, W., Germain, R. N. & Gerner, M. Y. Multiplex, quantitative cellular analysis in large tissue volumes with clearing-enhanced 3D microscopy (C e 3D). *Proc. Natl. Acad. Sci.* **114**, E7321–E7330 (2017).
127. Toni, L. S. *et al.* Optimization of phenol-chloroform RNA extraction. *MethodsX* **5**, 599–

608 (2018).

128. Chaturvedi, R. R. *et al.* Patterning Vascular Networks In Vivo for Tissue Engineering Applications. *Tissue Eng. Part C Methods* **21**, 509–517 (2015).
129. Nusse, R. & Clevers, H. Wnt/β-Catenin Signaling, Disease, and Emerging Therapeutic Modalities. *Cell* **169**, 985–999 (2017).
130. de Lau, W., Peng, W. C., Gros, P. & Clevers, H. The R-spondin/Lgr5/Rnf43 module: regulator of Wnt signal strength. *Genes Dev.* **28**, 305–316 (2014).
131. Kretzschmar, K. & Clevers, H. Wnt/β-catenin signaling in adult mammalian epithelial stem cells. *Dev. Biol.* **428**, 273–282 (2017).
132. Si-Tayeb, K., Lemaigre, F. P. & Duncan, S. A. Organogenesis and Development of the Liver. *Dev. Cell* **18**, 175–189 (2010).
133. Rocha, A. S. *et al.* The Angiocrine Factor Rspondin3 Is a Key Determinant of Liver Zonation Report The Angiocrine Factor Rspondin3 Is a Key Determinant of Liver Zonation. *CellReports* **13**, 1757–1764 (2015).
134. Gerbal-Chaloin, S. *et al.* The WNT/ β -Catenin Pathway Is a Transcriptional Regulator of CYP2E1, CYP1A2, and Aryl Hydrocarbon Receptor Gene Expression in Primary Human Hepatocytes. *Mol. Pharmacol.* **86**, 624–634 (2014).
135. Piraner, D. I. *et al.* Going Deeper: Biomolecular Tools for Acoustic and Magnetic Imaging and Control of Cellular Function. (2017). doi:10.1021/acs.biochem.7b00443
136. Hughes, A. J. *et al.* Engineered Tissue Folding by Mechanical Compaction of the Mesenchyme. *Dev. Cell* **44**, 165-178.e6 (2018).
137. Nimpf, S. & Keays, D. A. Is magnetogenetics the new optogenetics? *EMBO J.* **36**, 1643–1646 (2017).
138. Guo, Q. *et al.* Light activated cell migration in synthetic extracellular matrices. *Biomaterials* **33**, 8040–8046 (2012).
139. Toda, S., Blauch, L. R., Tang, S. K. Y., Morsut, L. & Lim, W. A. Programming self-organizing multicellular structures with synthetic cell-cell signaling. *Science (80-.).* **361**, 156–162 (2018).
140. Martyn, I., Kanno, T. Y., Ruzo, A., Siggia, E. D. & Brivanlou, A. H. Self-organization of a human organizer by combined Wnt and Nodal signaling. *Nature* **558**, 132–135 (2018).